MULTI-AXIS FIBER BRAGG GRATING ACCELEROMETER

by

Li Long

Submitted in partial fulfilment of the requirements
for the degree of Master of Applied Science

at

Dalhousie University
Halifax, Nova Scotia
June 2010

DALHOUSIE UNIVERSITY

ELECTRICAL AND COMPUTER ENGINEERING

The undersigned hereby certify that they have read and recommend to the Faculty of Graduate Studies for acceptance a thesis entitled "MULTI-AXIS FIBER BRAGG GRATING ACCELEROMETER" by Li Long in partial fulfilment of the requirements for the degree of Master of Applied Science.

Dated: June 8th, 2010

Supervisor:

Dr. Michael Cada

Readers:

Dr. Zhizhang (David) Chen

Dr. W. J. Phillips

DALHOUSIE UNIVERSITY

DATE: June 8, 2010

AUTHOR: Li Long

TITLE: Multi-axis Fiber Bragg Grating Accelerometer

DEPARTMENT OR SCHOOL: Electrical and Computer Engineering

DEGREE: M.A.Sc CONVOCATION: October YEAR: 2010

Permission is herewith granted to Dalhousie University to circulate and to have copied for non-commercial purposes, at its discretion, the above title upon the request of individuals or institutions.

_____

Signature of Author

TABLE OF CONTENTS

LIST OF TABLES

LIST OF FIGURES

LIST OF ABBREVIATIONS

Al_2O_3	Alumina
B_2O_3	Boron Oxide
FBG	Fiber Bragg Grating
FEM	Finite Element Method
GeO_2	Germania
ION	International Ocean Network
LPFGs	Long Period Fiber Gratings
MEMS	MicroElectroMechanical Systems
ONSFI	Ocean Network Seafloor Instrumentation
P_2O_5	Phosphorus Pentoxide
SiO_2	Silica Glass

ACKNOWLEDGEMENTS

This thesis was only possible with the support of many individuals. First of all, I would like to thank my supervisor, Dr. Michael Cada, Professor in the Department of Electrical and Computer Engineering at Dalhousie. His academic advice, encouragement, and patience are greatly appreciated.

Second, I would like to thank other reading committee members, Dr. Zhizhang (David) Chen, Professor in the Department of Electrical and Computer Engineering at Dalhousie, and Dr. W. J. Phillips, Professor and Head of the Department of Engineering Mathematics and Internetworking at Dalhousie.

Third, I would like to thank SEAformatics Group, a research group for The Ocean Network Seafloor Instrumentation (ONSFI) Project, for this research opportunity and financial support.

Furthermore, I would like to extend my thanks to team member, Nan (Jack) Wu, my colleage with whom I enjoyed my student life in the Photonics Group at Dalhousie.

Finally, I would like to thank my husband and my lovely son for supporting me during the entirety of my research.

ABSTRACT

The significant advantages of Fiber Bragg Grating, for example, wavelength encoded response, immunity to electromagnetic field, low cost, and multiplexing capability, have drawn great attention to optical fiber network devices in telecommunication and sensing technology development in civil and structural field. Adding/dropping filter elements in wavelength division multiplexing are a typical example of successful deployment of FBG in optical fiber communication networks. For sensing, FBG based transducers are widely used in a large structure (i.e. a bridge or a tall building) to monitor and track critical parameters, for example, temperature, pressure, or vibration. The required strain resolution and dynamic range of FBG transducers can vary from application to application.

This research was originally initiated by Ocean Network Seafloor Instrumentation (ONSFI) project. The main objective of this project is to develop proof-of-concept sensor nodes and associated power supply and networking software targeted at seismic wave detecting and geological imaging of ocean bottom as its primary application. This thesis mainly focuses on sensor nodes design. A small two-axis and three-axis accelerometer using optic fiber with FBG written in the core as sensing element were originally designed due to the advantages of FBG mentioned above. The proposed design has a concentrated mass sitting in the middle of a rigid frame, and a glass fiber with a FBG written in the fiber core as a stiff spring is connected between each side of the frame and the mass. The two accelerometers can decouple the ground motion along different axes, resulting in virtually zero cross-sensitivity, which exceeds currently available seismometers. The accelerometer or seismometer has a working bandwidth below the structure's natural frequency and linearly responds to ground movement. COMSOL Multiphysics by using Finite Element Method (FEM) was used to analyze and simulate the two devices.

In addition, the light traveling through a step-index single mode fiber was modeled by using COMSOL Multiphysics RF Module.

CHAPTER 1 INTRODUCTION

This chapter shall briefly introduce my research motivation, Fiber Bragg Grating fabrication methods, and FBG-based accelerometer development.

1.1 Motivation

Since 70% of the Earth's surface is covered by water, International Ocean Network (ION) Committee launched a long-term international plan in 1996 to install long-term ocean seismic stations to extend Global Seismic Network. The purpose of that plan was to extend Global Seismic Network to the sea floor to achieve more uniform coverage on the surface of the Earth for global structure and earthquake/seismicity studies. Although it is a more cost effective way to place a seismometer in the sediment, experience on land with Global Seismic Network stations indicates that the best results are obtained by placing the seismic sensors in a borehole at about 100 meters deep. There are two main advantages associated with this type of installation. First, a sensor set firmly in bedrock moves faithfully with the true motion of the solid earth. Secondly, the ambient noise levels are reduced considerably by getting away from the ocean surface. There are 21 potential sites established to install permanent borehole seismometer as listed in Table 1 because earthquake sources are essentially confined to plate boundaries. Plate boundaries are found at the edge of the lithospheric plates. Earthquakes, volcanoes, and tsunamis originate at the narrow boundary zones between the plates.

It is well known that the electro-magnetic seismometer has been widely used on continents, islands and ocean floors. It is an electromagnetic device in which a coil moves

in the field of a permanent magnet resulting from ground movement. The motion induces a voltage in the coil; then, the voltage detected at the receiver reflects the displacement of the ground. Calibrating a seismometer is critical to getting useful data. Techniques include weight-lift, shake-table methods, Willmore bridge method, and step-release-method. Despite the availability of these calibration methods, due to their complexity or difficulty, many users simply choose a less than satisfactory practice of using specification supplied by the manufacturer [1].

MEMS (MicroElectroMechanical Systems) accelerometers using commercial MEMS elements have been developed for trial use in seismic surveys by Takao AIZAWA et al. in Japan [2]. The results of their experiments and observations show that MEMS accelerometers have better sensitivity than conventional geophones used in seismic surveys. The characteristic of MEMS accelerometers used in earthquake observation in low frequency, however, is yet to be investigated. One of the disadvantages of MEMS accelerometers is that gravitational acceleration has to be calibrated.

In the last couple of decades, a variety of FBG based accelerometer designs exist that meet different applications. Each design, such as FiberSensing designed FS-6500 and Micron Optics designed OS 700-701 & OS 700-721, has different characteristics in terms of sensitivity, frequency range, and maximum detectable acceleration. Those accelerometers had comparative or better performance characteristics than those of traditional sensors. However, they are only good for single-axis acceleration measurement.

This research proposed a two-axis and three-axis Fiber Bragg Grating accelerometers/seismometers. The two-axis transducer is used to detect ground motion in up-down direction and east-west direction while the three-axis one is used to detect ground motion in three directions: up-down, east-west, and north-south. The proposed accelerometers will not require calibration; moreover, they will make a big difference in sensor complexity, network integration, and cross-sensitivity compared to conventional seismometers.

Table 1 ION Proposed Seafloor Borehole Seismic Observatories Location List (Data from ION website)

Ocean	Site	Latitude	Longitude
North Atlantic	Mid-Atlantic Ridge	51.0	-33.0
North Atlantic	Mid-Atlantic Ridge	1.0	-24.0
North Atlantic	Mid-Atlantic Ridge (B-DEOS)	37.25	-32.5
South Atlantic	Argentine Basin	-36.0	-34.0
South Atlantic	Atlantic-Indian Ridge	-52.0	15.0
South Atlantic	Walvis Ridge	-28.0	2.0
South Atlantic	East Scotia Ridge (B-DEOS)	-57.5	-27.5
Indian	Carlsberg Ridge	6.0	63.0
Indian	Mid-Indian Ocean Basin	-2.0	85.0
Indian	Wharton Basin/ Broken Ridge	-27.0	100.0

(Continuing from the previous page)			
Indian	Southeast Indian Ridge	-45.0	99.0
Indian	Southeast Indian Ridge	-51.0	132.0
North Pacific	Northeast Pacific Basin	43.0	-148.0
North Pacific	Northeast Pacific Basin	39.0	-171.0
Central Pacific	East Pacific Basin	10.0	-125
Central Pacific	East Pacific Rise	-11.0	-107.0
South Pacific	Peru Basin	-23.0	-90.0
South Pacific	East Pacific Rise	-41.0	-110.0
South Pacific	Southeast Pacific Basin	-59.0	-108.0
South Pacific	Southwest Pacific Basin	-37.0	-150.0
South Pacific	Pacific-Antarctic Ridge	-57.0	-155.0

1.2 Background

Silica glass (SiO_2) is the main material used for optical fibers. The typical value of refractive index of silica is 1.46, but it can be modified by doping which is obtained by adding impurities to the material. The refractive index profile is determined by the type and concentration of impurities. Dopants, Germania (GeO_2), Phosphorus pentoxide (P_2O_5), and alumina (Al_2O_3) are typically used to raise the refractive index of the core of silica fiber; alternatively, fluorine or boron oxide (B_2O_3) is used to lower the refractive index of the cladding.

A fiber Bragg Grating is a periodic perturbation of the refractive index along the fiber length in the fiber's core which is formed by exposure of the core to an intense optical interference pattern.

1.2.1 Fabrication Techniques

In 1978, Hill et al, first demonstrated the fabrication of optical waveguide filters in Ge-doped silica core fiber with the aid of a single mode argon-ion laser [3]. The argon-ion laser operated at 488.0 nm was launched into a Ge-doped fiber with a NA=0.2 and core diameter of 2.5μm. The back reflection of the fiber was observed at the time when a periodic structure was formed in the fiber, and the reflectivity grew with the increase of exposure time. The photosensitivity of Ge-doped fiber was unknown at that time, but it raised others' curiosity about finding the cause of photo induced refractive index change and how the wavelength of the light source effects grating fabrications. Currently, there

are three major methods for fabricating Fiber Bragg Grating: Transverse holographic method, phase mask method, and point-by-point method.

FBG fabricated by the interference of two coherent optical UV beams with a wavelength near 244nm was illustrated by Meltz, et al. in 1989 [4]. Their experimental setup is shown in Figure 1.2.1. A temporal and spatial coherent UV laser beam that lies in the 244nm band was split into two equal intensity beams at the beam splitter. Basically temporal coherence tells us how monochromatic a wave is and how the wave interferes with itself at a different time. Spatial coherence describes the correlation between signals at different points in space. The two beams, through two different paths, recombined within the fiber core producing an interference pattern, and the fiber was set up in a way that the interference pattern was normal to the fiber axis. The cylindrical lenses were used to focus the beams in order to increase the intensity of the pattern.

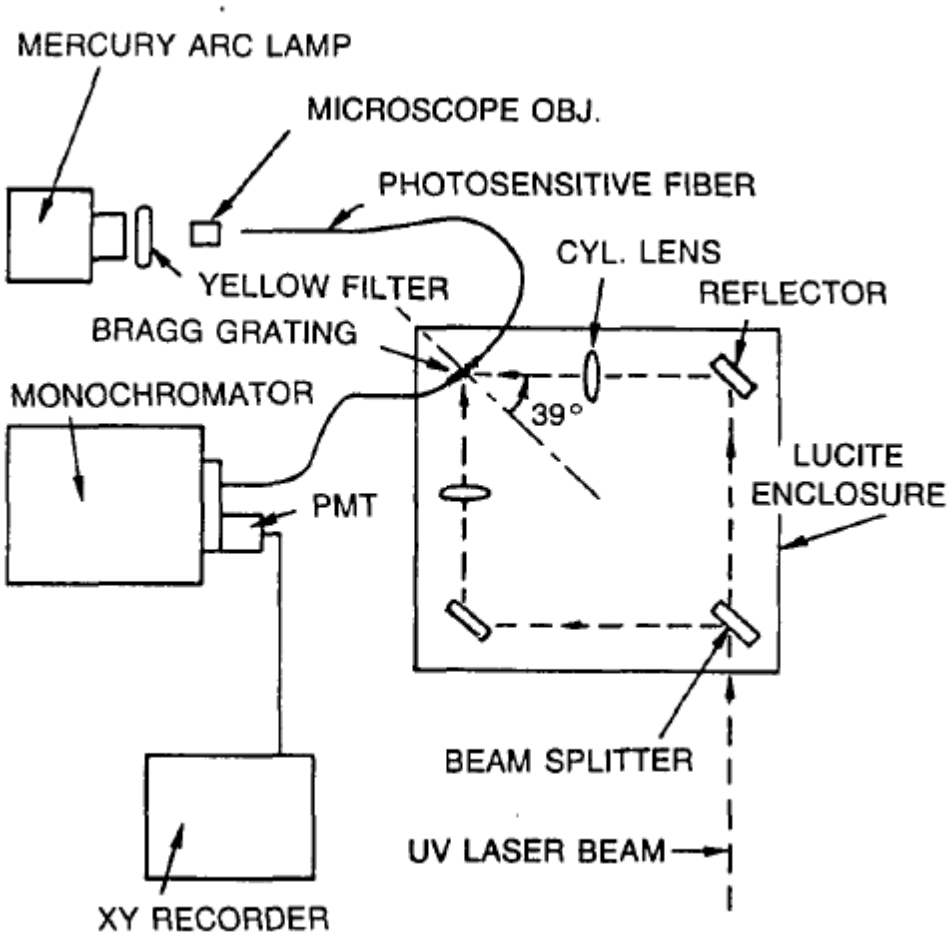

Figure 1.2.1: Diagram of transverse holographic experimental setup [4]

This transverse holographic technique used to form in-fiber Bragg gratings is more efficient and flexible when compared to the internal writing method in [3]. Moreover, the transverse holographic method is not length limited by saturation effects and can be tailored to a desired filter characteristic by shaping and tilting the writing pattern through control of the interference angle and divergence of the beams. This technique is possible because the fiber cladding is transparent to the ultraviolet light where the fiber core is highly absorbing to the ultraviolet light [5].

However, the quality of the interference fringe pattern produced by the transverse holographic method heavily relies on the coherence (spatial and temporal) of the UV beams, and the stability of the fringe pattern is influenced by the vibration of the setup. It is well understood that it is difficult to form a FBG repeatedly by using this method. The phase mask technique overcomes many of the problems associated with the transverse holographic technique. In 1993, Hill et al. showed that Bragg gratings could be fabricated by the phase mask grating [6]. The schematic of their experimental apparatus is illustrated in Figure 1.2.2. The fiber was placed where the interference pattern was generated behind the phase mask. The incident UV beam passed through the phase mask at a normal angle. The phase mask fabricated in a high quality fused silica flat structure transparent to the KrF excimer laser radiation with correct grating design, splits the incident beam into diffraction orders according to [7]:

$$\sin(\theta_{mPM}/2) = m\lambda_{UV}/\Lambda_{PM} + \sin\theta_i \tag{1.1}$$

Here,

m: Diffracted order with values of 0, $\pm 1, \pm 2, \pm 3 \ldots$;

θ_i : UV beam incident angle with respect to the normal to the phase mask;

θ_{mPM} : Diffracted angle at order m with respect to the normal to the phase mask;

Λ_{PM} : Period of the phase mask;

λ_{UV} : Wavelength of the incident UV light.

Usually a phase mask is designed to concentrate the diffracted power in +1,-1 orders, with above 35% of transmitted light each, and to suppress the diffracted power in 0 order, with below 5% of transmitted light.

The grating period in the fiber core is half of the period of the phase mask grating and is independent of the UV wavelength, according to the expression below:

$$\Lambda_G = \Lambda_{PM} / 2 = N\lambda_B /(2n_{eff}) \quad (1.2)$$

where,

Λ_G : Period of Fiber Bragg Grating

N: An integer indicating the order of the grating period with values of 1, 2…

$\lambda_{B:}$ Bragg wavelength

n_{eff}: Effective index of Fiber Bragg Grating

It should be noted that the period of the phase mask is relevant to the wavelength of the incident UV beam although the written grating period is independent of the UV wavelength.

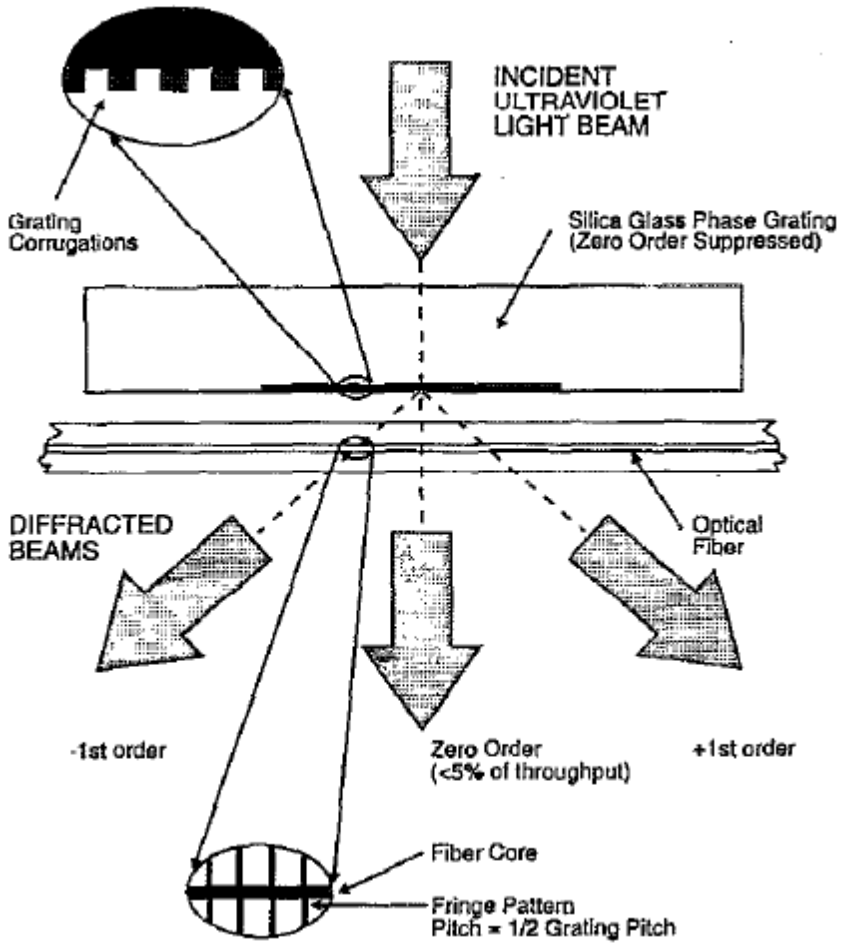

Figure 1.2.2: Schematic of the experimental apparatus for Bragg Grating writing by using phase mask [6]

The basic principle of the point-by-point technique is shown in Figure 1.2.3. The UV light laser pulse radiates on the optic fiber through the slit while the fiber moves by certain control; in this way, the refractive index of the core in the fiber is changed and the fiber grating is generated point-by-point. Gratings fabricated by this technique were demonstrated by Hill et al. in 1990 [8]. Two methods were used in their experiment to write the gratings: Fiber stayed still at each point and a single laser pulse impringed on

the fiber through the slit or the fiber moved continuously and the laser flashed at regular intervals. It turned out that stopping the fiber for each point gave better results. This grating fabrication technique is not very efficient with gratings having so many periods. Also, it has only been used to write Long Period Fiber Gratings (LPFGs) due to the fact that it is difficult to focus a clean slit of UV light of sub-micron dimensions.

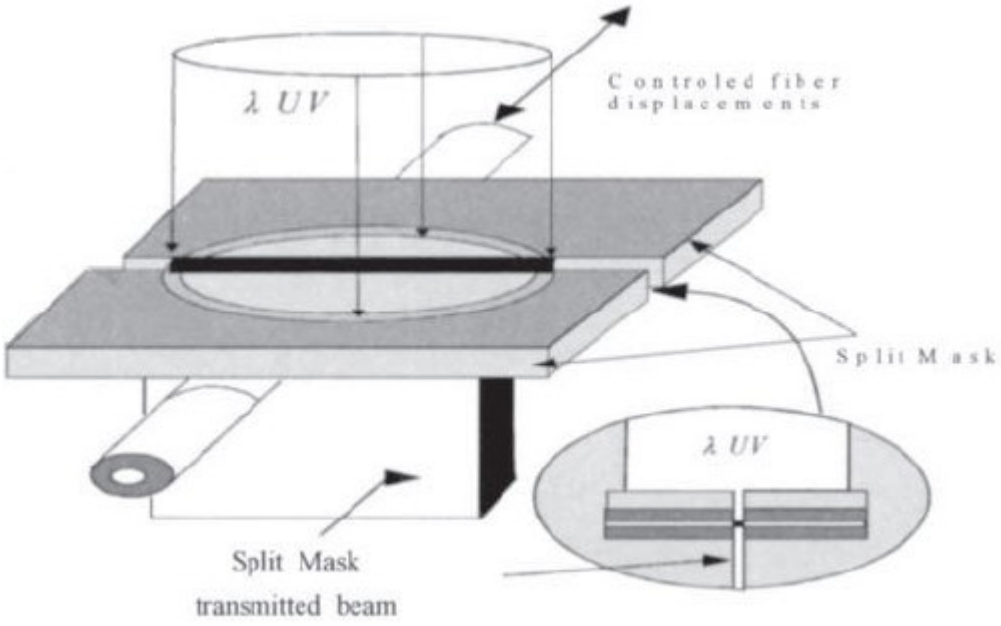

Figure 1.2.3: Basic principle of the point-by-point technique [8]

1.2.2 FBG-based Accelerometers

Over the last 30 years, significant research effort and progress has been achieved in the development of FBG accelerometers. Typically, these accelerometers function by a coupling between an inertial mass vibration and the induced strain within the FBG. A FBG based accelerometer, which was made with two parallel rectangular plates with a mass in the middle and a FBG attached to the bottom of the plate, was introduced in [9]. The transducer is shown as Figure 1.2.4. The dual flexural beams were used to minimize

cross-sensitivity. The advantage of this structure is to have low cross-axis sensitivity and good acceleration sensitivity. The disadvantage is that the grating needs to be as short as possible to reduce the averaging effects imposed by its finite length and to minimize strain gradient-induced spectral broadening.

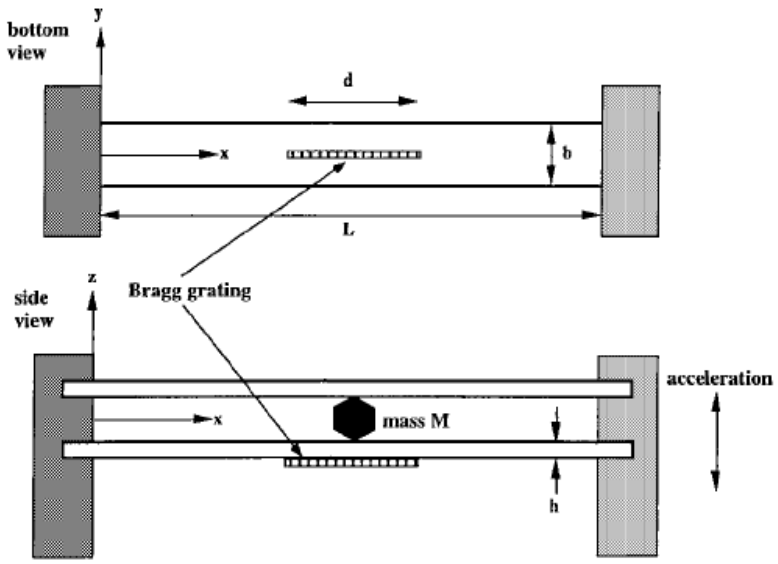

Figure 1.2.4: A schematic of the beam-plate design

A FBG-based accelerometer with a different design is presented in [10]. The system consists of a cantilevered beam and a mass as shown in Figure 1.2.5. A Bragg grating element is not directly glued to a cantilever to avoid possible non-uniform strain in the element. The advantage of this structure is the Bragg grating element is always subject to uniform strain distribution along its measuring length resulting in a sharp reflection characteristic with no broadening in its reflection spectrum. However, the Bragg grating element needs to be pre-tensioned to achieve a uniform strain distribution.

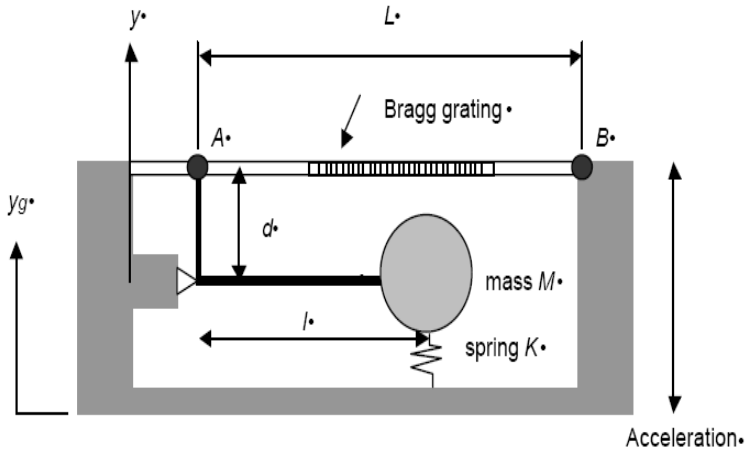

Figure 1.2.5: Mechanism of FBG accelerometer

Although there are many other different designs that have been used in the FBG-based accelerometer designs, such as leaf spring used in [11], they all are a single-axis acceceleromeeter, which means they can only detect acceleration in a single direction. In this thesis, the main focus is on developing a multi-axis FBG-based transducer with the same detecting machanism on each axis. The structure has high sensitivity and low cross-sensitivity.

1.3 Organization of the thesis

The thesis is organized as follows. Chapter 2 presents FBG sensors sensing principles. A basic knowledge of step-index fiber and FBG is introduced. Chapter 3 describes the proposed two-axis transducer and three-axis transducer. The theoretical calculation of resonant frequency and sensitivity of the structures are analyzed. Chapter 4 presents the finite element method and the modeling results of those two transducers. Chapter 5 is

devoted to the finite element method modeling of step index fiber. Finally, the thesis is summed up and future research direction is put forward in Chapter 6.

CHAPTER 2 FBG SENSORS SENSING PRINCIPLE

To know how a FBG can diffract incident light at one wavelength and transmit the others, it is important to understand the fundamentals of step-index fiber first.

2.1 Guided Modes in Optical Fibers and Resonant Coupling in Fiber Bragg Gratings

An optical fiber is a medium used to transmit light from a source to a detector. The step-index fiber consists of a central core whose refractive index is n_1, surrounded by a cladding whose refractive index is n_2. The possible behaviors of the incoming light at the boundary between the core and the cladding depend on the incident angle θ, as shown in Figure 2.1.1 [12].

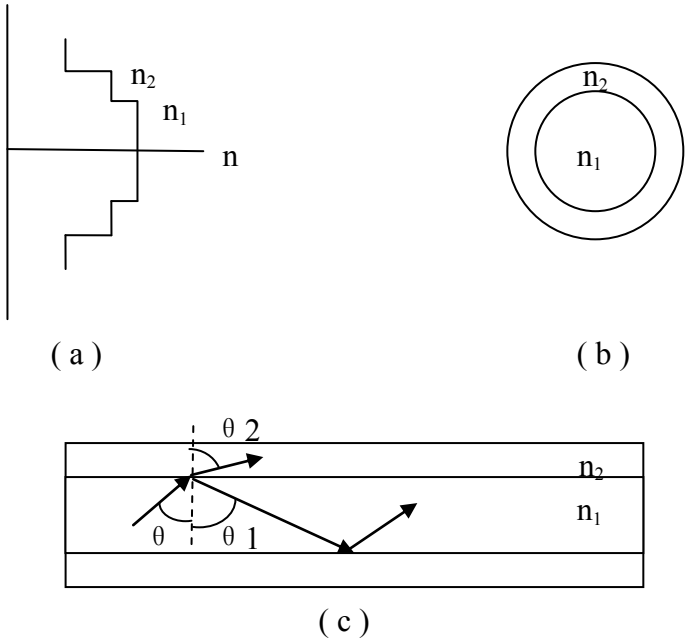

Figure 2.1.1: Schematic of an optical fiber. (a) Refractive index profile. (b) End view. (c) Cross-sectional side view.

From the law of reflection and the law of refraction, the following relationship shall hold:

$$\theta = \theta_1 \quad \text{(Law of reflection)}$$

$$n_1 \cdot \sin(\theta) = n_2 \cdot \sin(\theta_2) \quad \text{(Law of refraction)} \tag{2.1}$$

when θ is equal to a certain angle, θ_2, the lost part of the light goes along the boundary between the core and the cladding ($\theta_2 = 90^o$). By substituting $\theta_2 = 90^O$ into equation (2.1), we get:

$$n_1 \cdot \sin(\theta_c) = n_2 \cdot \sin(90^0) = n_2 \tag{2.2}$$

$$\sin(\theta_c) = \frac{n_2}{n_1} \tag{2.3}$$

Here, θ_c is called the critical angle. To obtain a total internal reflection, there are two conditions that must be met:

- The refractive index n_1 of the core must be larger than the refractive index n_2 of the cladding.
- The incident angle θ must be greater than the critical angle θ c.

In the case of common single mode fiber, the fundamental core mode LP_{01} is described by using the linearly polarized approach and it can be found by solving the following equation [13]:

$$V\sqrt{1-b}\,\frac{J_1(V\sqrt{1-b})}{J_0(V\sqrt{1-b})} = V\sqrt{b}\,\frac{K_1(V\sqrt{b})}{K_0(V\sqrt{b})} \tag{2.4}$$

where,

$$V = \frac{2\pi r_{co}}{\lambda}\sqrt{n^2_{co} - n^2_{cl}} \tag{2.5}$$

$$b = \frac{n^2_{eff} - n^2_{cl}}{n^2_{co} - n^2_{cl}} \tag{2.6}$$

V: The normalized frequency, which determines the number of the modes in the core;

J_n: A Bessel function of the first kind;

K_n: A modified Bessel function of the second kind;

r_{co}: The core radius;

λ : The light wavelength in vacuum;

n_{co}: The refractive index of the core;

n_{cl}: The refractive index of the cladding;

n_{eff}: The effective refractive index of the core.

In fact, if there are refractive index perturbations in the core along the fiber axis, the modes can be coupled to other modes. Fiber gratings can be classified into two categories based on the coupling direction. One type is called short period grating or Fiber Bragg Grating based on the traveling direction of modes coupled to each other. The traveling direction of coupled modes is opposite in this type of grating. The second type is called transmission grating, represented by LPFGs (long Period Fiber Gratings), where core modes are coupled to cladding modes. By adding a periodic variation to the fiber core, light travelling between media of different refractive indices may be reflected and refracted at the interface as illustrated in Figure 2.1.2, which shows contradirectional coupling resulting from a short period type of gratings.

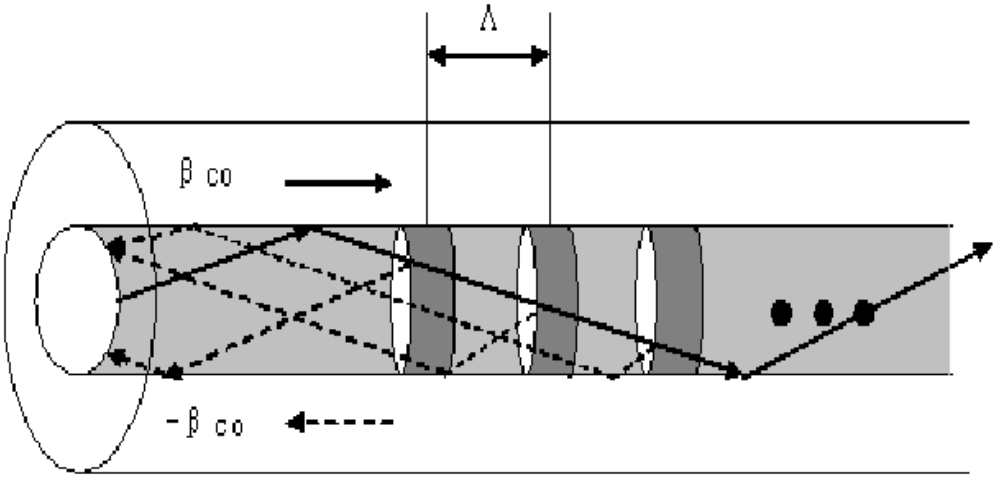

Figure 2.1.2: Contradirectional coupling

For the diffracted mode to be accumulated constructively, each diffracted light from the series of the perturbation should be in phase, which means the following phase matching condition should be satisfied:

$$\beta_i - (\pm\beta_d) = \frac{2\pi}{\Lambda} m \tag{2.7}$$

where

β_i is the propagation constants for the incident modes;

β_d is the propagation constants for the diffracted modes;

Λ is the period of the grating;

m is an integer number.

A minus sign before the propagation constant describes the case wherein the mode propagates in the –z direction. The optical path difference between light diffracted from the adjacent grating positions should be an integer multiple of the wavelength for a

resonant coupling of modes. In most cases, first-order diffraction is dominant, and hence m is assumed to be unity. Based on the relationship between the propagation constant and the wavelength, the resonant wavelength can be obtained as follows:

$$\beta_i = \kappa_0 n_{i,eff} \tag{2.8}$$

$$\beta_d = \kappa_0 n_{d,eff} \tag{2.9}$$

$$\kappa_0 = \frac{2\pi}{\lambda} \tag{2.10}$$

$$\lambda = [n_{i,eff} - (\pm n_{d,eff})]\Lambda \tag{2.11}$$

In the case of contradirectional coupling in a single-mode fiber, the Bragg wavelength of the core mode is given by:

$$\lambda = 2 n_{co,eff} \Lambda \tag{2.12}$$

where,

$n_{co,eff}$: The effective index of the core mode.

2.2 Sensing Principles of FBG Sensors

Any physical change in optic fiber, such as strain, temperature, pressure, or polarization, which varies the refractive index or grating period, will change the Bragg wavelength. The measurand can be encoded in the Bragg wavelength, seen as a narrow band reflection or a dip in the transmission. Shifts in the spectrum are independent of the optical intensity. The Bragg wavelength shift due to strain and temperature can be governed by this general equation with appropriate coefficients [13]:

$$\delta\lambda_\beta / \lambda_\beta = (CT\lambda_\beta)\delta T + (C\varepsilon\lambda_\beta)\delta\varepsilon + (CP\lambda_\beta)\delta P \quad (2.13)$$

where,

$CT\lambda_\beta$: The temperature Bragg wavelength coefficient;

$C\varepsilon\lambda_\beta$: The strain Bragg wavelength coefficient;

$CP\lambda_\beta$: The hydrostatic pressure Bragg wavelength coefficient.

They are calculated for fiber optic devices as follows:

$$CT\lambda_\beta = (\alpha + \zeta) \quad (2.14)$$

$$C\varepsilon\lambda_\beta = (n_{co,eff}{}^2 / 2)[p_{12} - \mu(p_{11} + p_{12})] = [1 - P_e] \quad (2.15)$$

$$\lambda_\beta[CP\lambda_\beta] = \varepsilon_z - (n_{co,eff}{}^2 / 2)[p_{11}\varepsilon_r + p_{12}(\varepsilon_z + \varepsilon_r)] \quad (2.16)$$

where,

$\alpha = (1/\Lambda)(\delta\Lambda / \delta T)$: Expansion coefficient of the fiber material;

$\zeta = (1/n_{co,eff})(\delta n_{co,eff} / \delta T)$: Thermo-optic coefficient of the fiber material;

μ : Poisson ratio;

p_{11} and p_{12}: elasto-optic tensor coefficients (Pockel's coefficients) along the direction 1 (fiber axis) and 2, respectively;

ε_z : Axial strain Poisson coefficient;

ε_r : Transversal strain Poisson coefficient;

P_e: A photoelastic constant of isotropic fiber and the average value is 0.22.

Typical reported values of 11pm/^{o}C (temperature sensitivity), 1.13pm/$\mu\varepsilon$ (strain sensitivity), and -3.5pm/Mpa (hydrostatic pressure sensitivity) have been deduced at a wavelength of 1550nm.

In this thesis, the focus is mainly on the transducer design which will be able to convert ground motion into strain change in a fiber within a FBG written in the core. A Bragg wavelength change caused by the strain will be detected if a receiving system is set up. In the next chapter, theoretical analysis of a proposed two-axis accelerometer and a proposed three-axis accelerometer will be presented.

CHAPTER 3 FBG ACCELEROMETER

A two-axis and three-axis FBG accelerometers are proposed in this chapter. The idea behind it is that a single-mode fiber with a FBG written in the core will be used as a spring element. The movement of the mass, which is connected to the fiber, will result in the change in fiber grating period; correspondingly, the change in grating period causes the strain change in the FBG. .

3.1 A Spring-Mass System

Suppose a mass, m, is attached to a spring, which in turn is suspended in a rigid case as shown Figure 3.1.1. A single degree of freedom system is utilized to study the forced vibration. By common definition, a single degree of freedom system is one for which only a single independent coordinate is needed to describe the motion of the system completely.

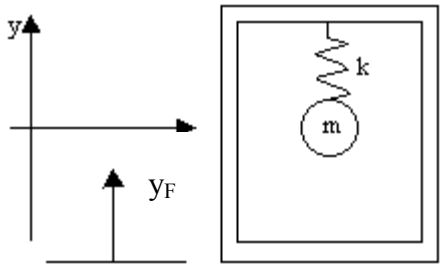

Figure 3.1.1: Mass-spring-damper system with movable support

Let y correspond to the motion of the mass and let y_F represent the motion of the rigid case. The associated kinetic diagram for the system is displaced in Figure 3.1.2. Since the spring force is proportional to the relative displacement of the mass with respect to

the case, and the damping force is proportional to the relative velocity of the mass with respect to the case, the equation of motion is found from Newton's Second Law as follows:

$$-k(y - y_F) - c(\dot{y} - \dot{y}_F) = m\ddot{y} \tag{3.1}$$

$$\ddot{y} + 2\omega_n \cdot \zeta \cdot (\dot{y} - \dot{y}_F) + \omega_n^2 \cdot (y - y_F) = 0 \tag{3.2}$$

where,

$$\omega_n = \sqrt{\frac{k}{m}}$$

$$\zeta = \frac{c}{2\sqrt{mk}}$$

m: Mass (kg);

c: Damping constant (N.s/m);

k: Spring constant (N/m).

Let u measure the displacement of the mass relative to the moving case, and hence measure the stretch in the spring. Here, y, y_F, and u are the function of time, t. Therefore,

$$u(t) = y(t) - y_F(t) \tag{3.3}$$

It then follows that $\dot{u}(t)$ represents the relative velocity of the mass with respect to the rigid case. Substitution of Equation (3.3) into Equation (3.2) gives the governing equation in terms of the relative motion of the mass as:

$$\ddot{u} + 2\omega_n\zeta\,\dot{u} + \omega_n^2 u = -\ddot{y}_F(t) \tag{3.4}$$

$\ddot{y}_F$ represents the acceleration of the rigid case.

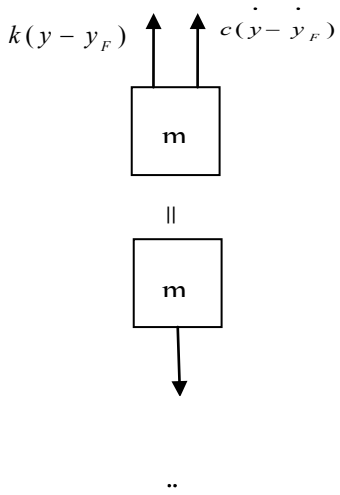

Figure 3.1.2: Kinetic diagram for system with support motion

Suppose the support case is subject to ground acceleration a_g, for example, a common sinusoidal force in nature, at y direction, the mass shall displace from its equilibrium position.

$$a_g = A_g \sin(\omega t) \tag{3.5}$$

$$\ddot{u} + 2\omega_n \zeta \dot{u} + \omega_n^2 u = -A_g \sin(\omega t) \tag{3.6}$$

The steady state solution of this problem can be written as:

$$u = U \sin(\omega t - \varphi) \tag{3.7}$$

where,

$$U = \frac{-1}{\sqrt{(1 - (\omega / \omega_n)^2)^2 + (2\xi(\omega / \omega_n))^2}} \frac{1}{\omega_n^2} A_g \tag{3.8}$$

$$\varphi = \tan^{-1}\left(\frac{2\xi(\omega / \omega_n)}{1 - (\omega / \omega_n)^2}\right) \tag{3.9}$$

Here,

Natural frequency $$\omega_n = \sqrt{k/m} \tag{3.10}$$

The result states that the mass will oscillate at the same frequency, ω, of the excitation, but with a phase shift φ. A normal strain ε exists in the spring as it is extended or compressed over its equilibrium length:

$$\varepsilon = \frac{\Delta U}{U} \tag{3.11}$$

If this spring is replaced by a single mode fiber with a Fiber Bragg Grating written in the core, a normal strain will be produced in the FBG element in the same manner as a ground motion moves the rigid case. The strain variation causes the shift of the Bragg wavelength accordingly.

Our objective is to design a FBG transducer capable of detecting and measuring seismic data at the seafloor which has:

- frequency range is 1Hz～200Hz;
- capability of sensing three axes with uniform sensitivity and low cross-sensitivity (> 26dB);
- the lowest resolvable acceleration 4mm/s2 (peak-to-peak ground amplitude 0.1mm@ 1Hz);
- maximum acceleration 40m/s2;
- dynamic range 80 dB.

The sensitivity of the transducer indicated here is its ability to convert the ground acceleration into wavelength shift in the FBG.

3.2 Two-axis FBG Accelerometer

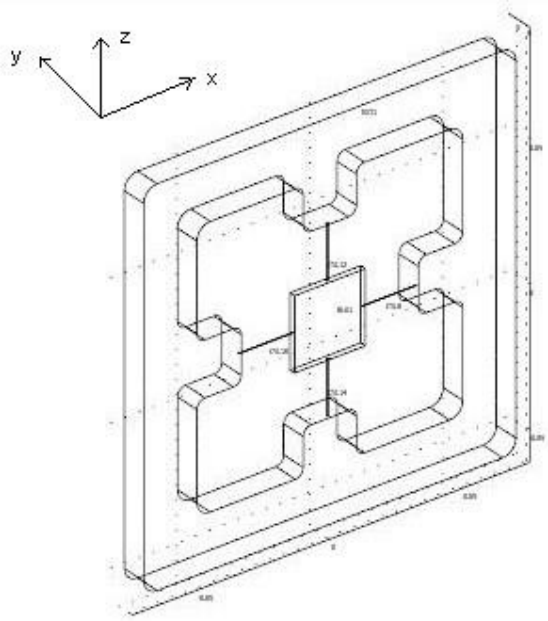

Figure 3.2.1: Proposed two-axis FBG transducer

In the figure above, a proof mass is centered within the external frame. Four optic fiber sections, each with a FBG written in the fiber core, are connected between the proof mass and the frame and are arranged to exert a reaction force on the proof mass in response to displacement of the proof mass along the sensing axis.

When the mass is subject to ground acceleration, a_g, the mass moves in the opposite direction of the acceleration. Suppose this sensor is only subjected to ground acceleration along z-axis, the mass movement causes two FBGs in z axis to be stretched and to be compressed, respectively. The system can be modeled by a single-degree-of-freedom system. The stiffness of the fiber elements along sensing axis z is represented by K1,

while the stiffness of the fiber elements in cross-axis x by K2. K1 and K2 can be written as:

$$K_1 = \frac{E_1 \cdot A}{L} \tag{3.12}$$

$$K_2 = \frac{3E_1 \cdot I}{L^3}, I = \frac{\pi \cdot r^4}{4} \tag{3.13}$$

where,

A: Cross sectional area of the fiber;

r: Fiber radius with a value of 62.5 μ m;

L: Effective length of each optic fiber section.

The natural frequency f of the system is:

$$f_n = \frac{1}{2\pi}\sqrt{\frac{2K_1 + 2K_2}{m}} \tag{3.14}$$

The parameters employed of this device are in Table 2:

Table 2: Fiber and Mass Parameters of the Two-axis FBG Transducer

Fiber Parameters			
Parameter	Description	Value	Unit
d	Single mode fiber diameter	0.125	mm
E1	Young's modulus of optic fiber	73.1	GPa
ν	Poisson Ratio	0.17	
L	Effective fiber length	20	mm
Mass Parameters			
Parameter	Description	Value	Unit
m	Proof mass	12.4	g
E2	Young's modulus of stainless steel	200	GPa
ν	Poisson Ratio	0.29	

Based on Equations (3.12), (3.13), and (3.14) along with Table 2, the natural frequency of this two-axis accelerometer is calculated as 428Hz.

Accordingly, the normal strain change on each fiber section is obtained by dividing Equation (3.8) by L:

$$\varepsilon = -\kappa A_g \tag{3.15}$$

In which the sensitivity κ is defined by the following expression:

$$\kappa = \frac{1}{\sqrt{(1-(\omega/\omega_n)^2)^2 + (2\xi(\omega/\omega_n))^2}} \frac{1}{\omega_n^2} \frac{1}{L} \tag{3.16}$$

The strain on the isotropic fiber gratings causes the Bragg wavelength to shift and is given by,

$$\Delta\lambda / \lambda_B = (1 - P_e)\varepsilon \tag{3.17}$$

The theoretical frequency response is calculated based on Equation (3.8) by using MATLAB and is shown as Figure 3.2.2.

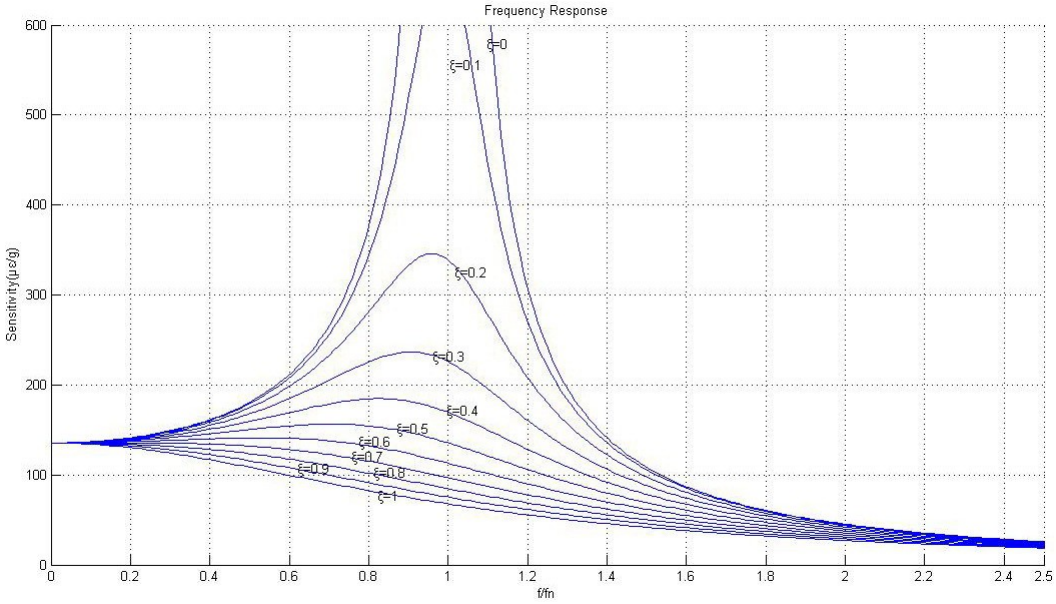

Figure 3.2.2: Two-axis transducer theoretical frequency response

In Figure 3.2.2, it is understood that within the range of f/fn $\leqslant$0.2, the response of the transducer is essentially independent of the excitation frequency f, and the output of the sensor is within a specified deviation, typically +/- 5% [14].

3.3 Three-axis FBG Accelerometer

Figure 3.3.1 shows the proposed three-axis FBG accelerometer.

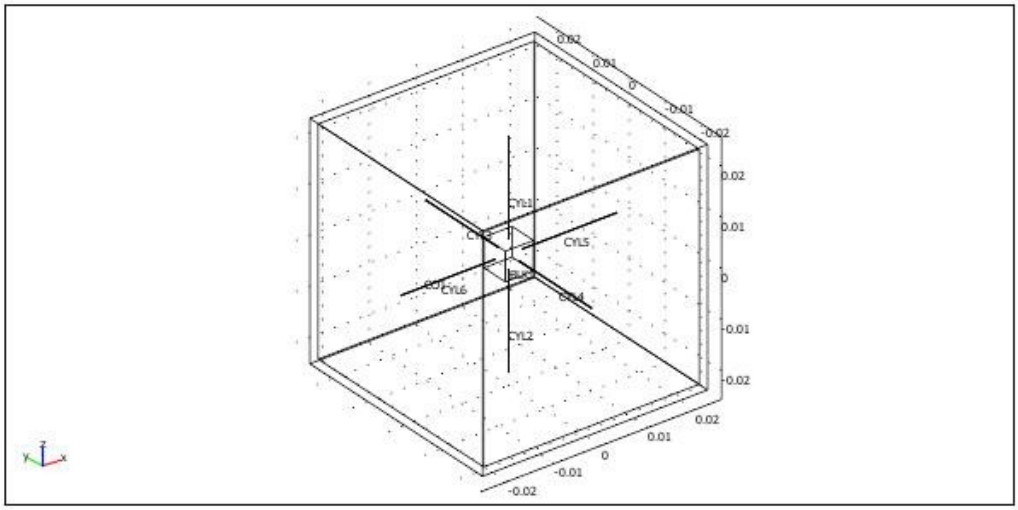

Figure 3.3.1: A proposed three-axis FBG transducer

Although the two structures look a bit different, the same method used in the two-axis transducer study can be applied here to analyze the strain change on the FBGs. The inertial mass stretches or compresses two FBGs in the same axis and causes their Bragg wavelength to shift in proportion to acceleration subjected. Suppose this sensor is only subjected to ground acceleration along z-axis, it can be modeled by a single-degree-of-freedom system.

The stiffness of the fiber elements along sensing axis z is represented by K1, while the stiffness of the fiber elements in cross-axes by K2. K1 and K2 can be written as

$$K_1 = \frac{E_1 \cdot A}{L} \tag{3.18}$$

$$K_2 = \frac{3E_1 \cdot I}{L^3}, I = \frac{\pi \cdot r^4}{4} \tag{3.19}$$

The natural frequency f of the system is expressed by,

$$f_n = \frac{1}{2\pi}\sqrt{\frac{2K_1 + 4K_2}{m}} \tag{3.20}$$

The parameters of this device are given in Table 3.

Table 3: Fiber and Mass Parameters of the Three-axis FBG Accelerometer

Fiber Parameters			
Parameter	Description	Value	Unit
d	Single mode fiber diameter	0.125	mm
E1	Young's modulus	73.1	GPa
ν	Poisson Ratio	0.17	
L	Effective fiber length	20	mm
Mass Parameters			
Parameter	Description	Value	Unit
m	Proof mass	2	g
E2	Young's modulus	200	GPa
ν	Poisson Ratio	0.29	

Based on Equations (3.18), (3.19), and (3.20) along with Table 3, the natural frequency of this tri-axis accelerometer is calculated as 1023Hz.

The normal strain changes over the fiber in the sensing axis are the same as the two-axis device based on Equation (3.11) except for the difference in the natural frequency. The

sensitivity due to different damping ratio based on Equation (3.8) is shown in Figure 3.3.2.

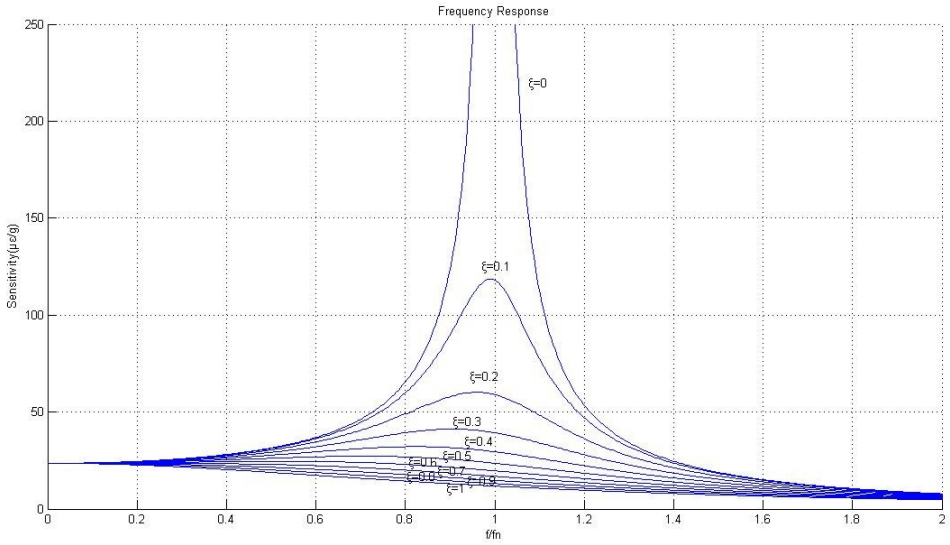

Figure 3.3.2: Three-axis transducer theoretical frequency response

In the next chapter, Finite Element Method will be introduced and simulation results of those two FBG accelerometers will be presented.

CHAPTER 4 FINITE ELEMENT METHOD AND MODELING RESULTS

In this chapter the modeling results of the two-axis and three-axis accelerometers will be presented. The modeling method is the finite element method, which is implemented in COMSOL Multiphysics.

4.1 Finite Element Method

The finite element method (FEM) is a computational technique used to obtain approximate solutions of boundary value problems in engineering [15]. A simple description of the FEM would be that it is a method where a structure is split into tens of thousands of fragments (finite elements). The behavior of each element is then represented using a simple equation. Finally, all the elements are reconnected. The resulting simultaneous algebraic equations (often in thousands) are then solved with the use of a computer. The result is the FEM output for the entire structure.

4.1.1 Procedure of FEM

COMSOL Multiphysics is this kind of software that uses FEM to model engineering problems in almost every engineering field. It is used to analyze the two-axis and three-axis accelerometers. To set up a model in COMSOL Multiphysics, there are conceptually six stages:

1) Drawing. It means specifying the domain(s) and constructing the geometries.

2) Mathematical equations. It means choosing appropriate pre-built application mode if it is available in the library or linking several application modes together.

3) Material properties of the geometries. It means defining material properties, loadings, and physical conditions which may include subdomain, boundary, edge, and even point constraints.

4) Meshing. It means choosing the element types to be used (e.g. triangular, rectangular, or irregular) and meshing the geometries on the purpose of connecting all the elements together.

5) Solving. COMSOL Multiphysics assembles the governing algebraic equations in matrix form and computes the unknown values of the primary field variable(s).

6) Postprocessing. Analysis and evaluation of the solution results is referred to as postprocessing. Sound engineering judgment shall be applied in determining whether the solution results are physically reasonable.

4.1.2 Dynamic Analyses

The equation of motion of a finite element model of a structure is:

$$[M]\{\ddot{q}\} + [C]\{\dot{q}\} + [K]\{q\} = \{F(t)\} \tag{4.1}$$

where,

$[M]$,$[C]$ and $[K]$ are the system mass matrix, viscous damping matrix and stiffness matrix, respectively, $\{q\}$ is the column matrix of the actual nodal displacement and $\{F(t)\}$ is the column matrix of the time-varying force.

The element equation of motion is:

$$\left[m^{(e)}\right]\left\{\ddot{u}\right\}+\left[c^{(e)}\right]\left\{\dot{u}\right\}+\left[k^{(e)}\right]\{u\}=\left\{f^{(e)}\right\} \tag{4.2}$$

Where $\{u\}$ is the column matrix (vector) of nodal displacements.

Next, the simulation results of these two-axis and three-axis transducers by using COMSOL Multiphysics with this motion finite element model are presented.

4.2 Simulation Results of Two-axis Accelerometer

The characteristics of an accelerometer can be seen from its frequency response, response to external acceleration, and from its cross-sensitivity.

4.2.1 Frequency Response

Frequency response is the measure of any system's output spectrum in response to an input signal. It is typically characterized by the magnitude of the system's response, and the phase, versus frequency. The COMSOL mesh grid of the device is as Figure 4.2.1. The simulated frequency response of our proposed two-axis transducer is shown in Figure 4.2.2, Figure 4.2.3, and Figure 4.2.4.

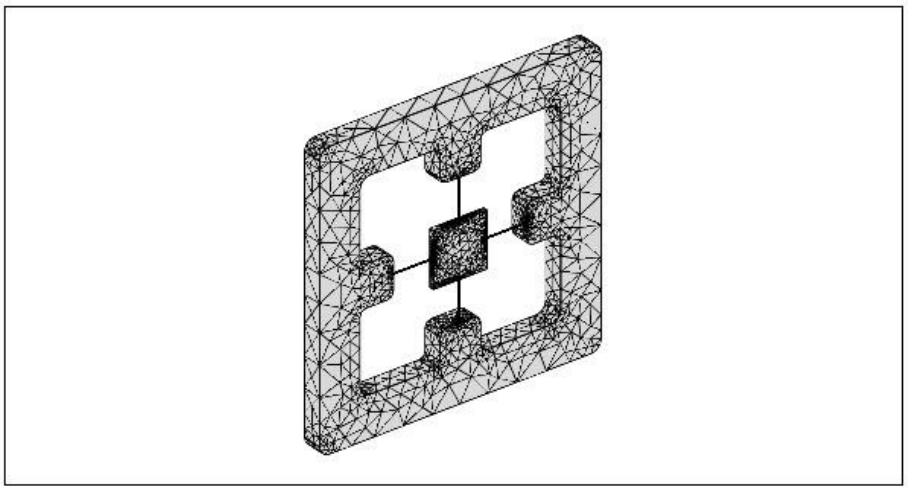

Figure 4.2.1: COMSOL mesh grid of the two-axis accelerometer

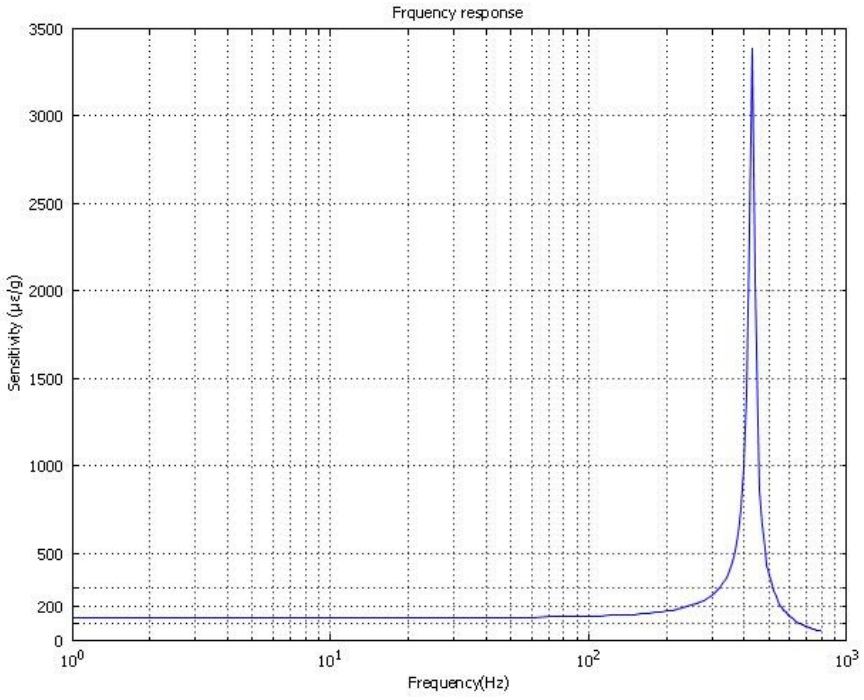

Figure 4.2.2: Sensitivity of the two-axis transducer as a function of frequency

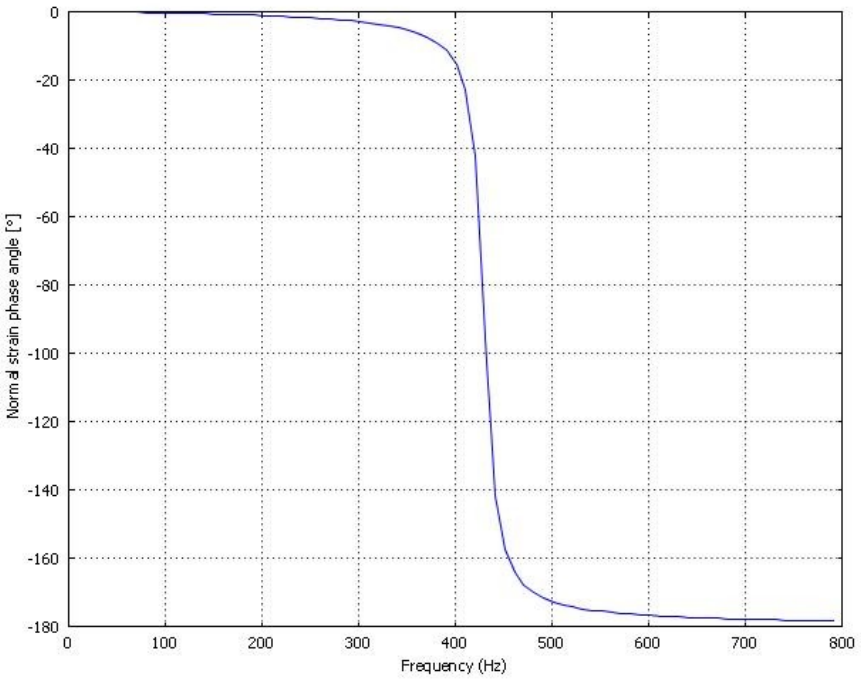

Figure 4.2.3: Phase angle in the upper fiber as a function of frequency of the two-axis accelerometer

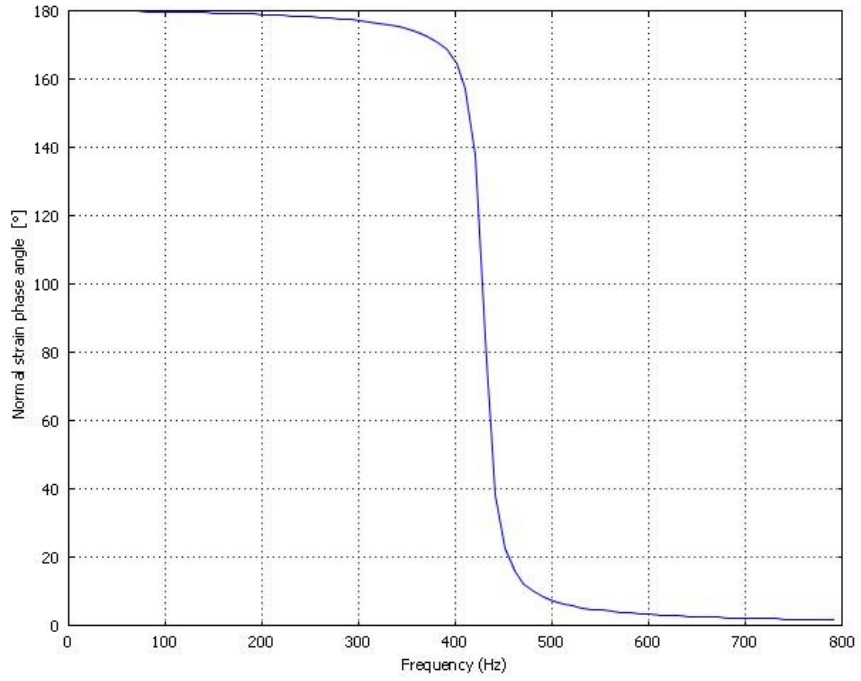

Figure 4.2.4: Phase angle in the lower fiber as a function of frequency of the two-axis accelerometer

As indicated in Figure 4.2.2, the simulation result is in good agreement with the theoretical values. The natural frequency 426Hz of the two-axis transducer is quite close to the calculated value 428Hz. The sensitivity is the same as that predicted in Figure 3.2.2 using Matlab. It can be seen from Figure 4.2.3 and Figure 4.2.4 that at resonant frequency 428Hz the phase angle is $\pm \pi/2$.

4.2.2 Harmonic Excitation Response

Harmonic excitation is an important class of forcing in the study of accelerations, both fundamentally and with regard to applications. If the system is simultaneously subjected to more than one force, the response of the system is equal to the sum of the responses to all the forces acting individually. In this thesis, one force acting on the structure was studied. Within a specified deviation, typically +/- 5%, the detectable frequency range of this transducer is about 1～85Hz based on the natural frequency of 426 Hz.

At first, the strain outputs in the fiber corresponding to the lowest resolvable acceleration 4mm/s2 (peak-to-peak ground amplitude 0.1mm@ 1Hz) in the form of sine function were examined. The normal strain change at each point in the upper fiber and in the lower fiber in z-axis is shown in Figure 4.2.5 and Figure 4.2.6. It is seen that the system oscillates at the frequency of the excitation as the damping ratio of the structure is small, here 0.05. The peak normal strain change in each portion of the fiber is about 0.028με, which will cause approximately 0.03pm wavelength shift at Bragg wavelength of 1550nm based on Equation (3.17) with the condition that the transducer experiences constant pressure and temperature. The boundary displacement of the device at t=2.4s is shown in Figure 4.2.7.

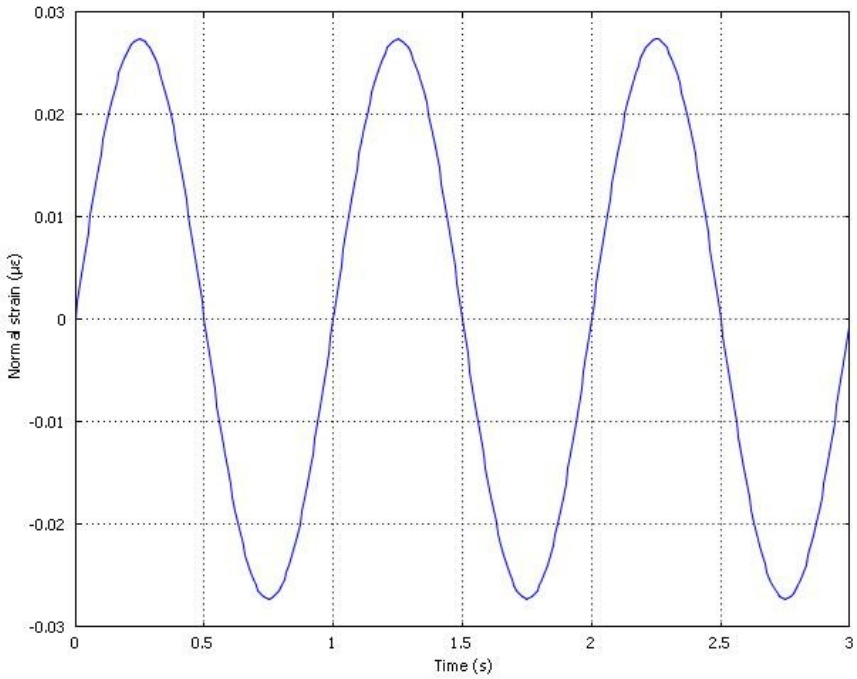

Figure 4.2.5: Normal strain change in the upper fiber at z-axis of the two-axis accelerometer corresponding to 4mm/s2 @1Hz

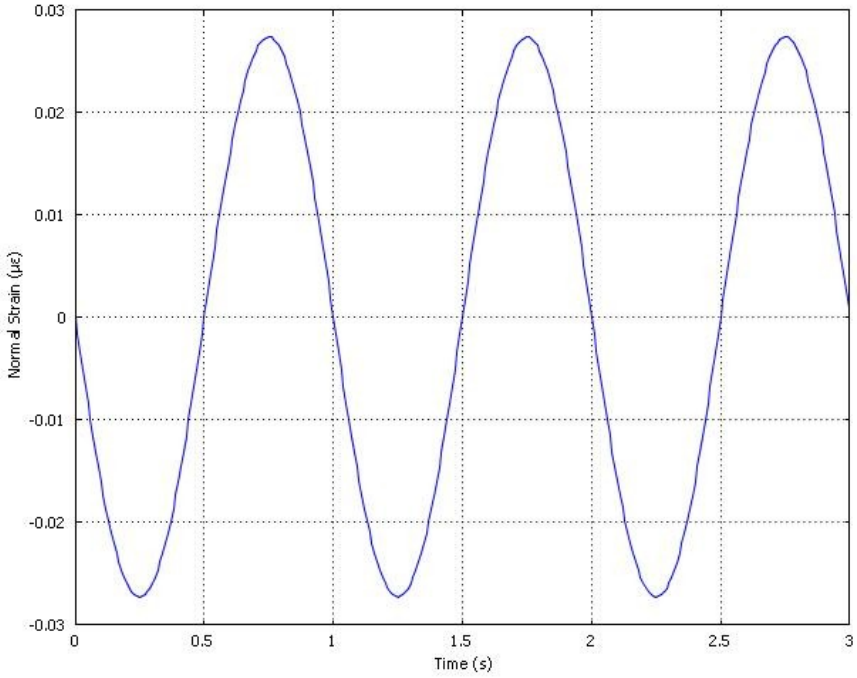

Figure 4.2.6: Normal strain change in the lower fiber at z-axis of the two-axis accelerometer corresponding to 4mm/s2 @1Hz

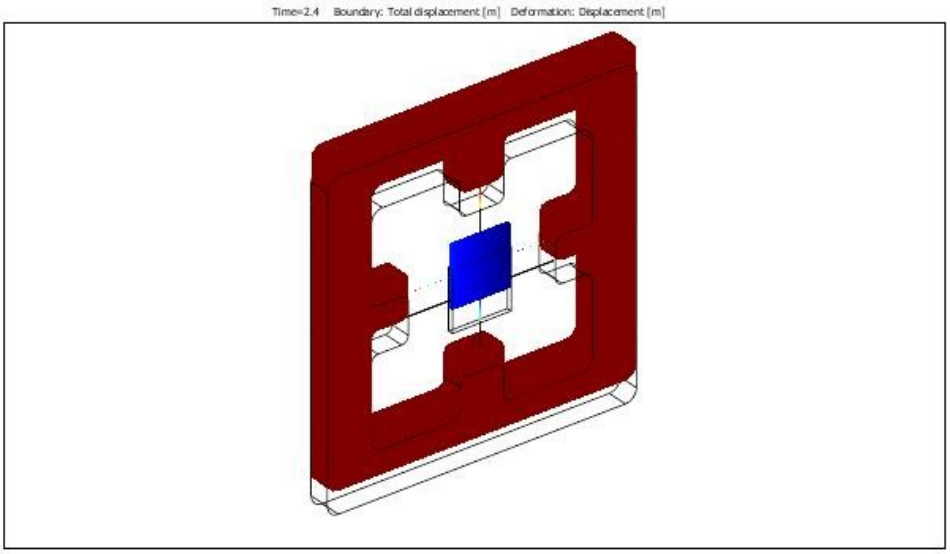

Figure 4.2.7: Boundary displacement at t=2.4s of the two-axis accelerometer corresponding to 4mm/s2 @1Hz

Next, the strain outputs in the fiber corresponding to the lowest resolvable acceleration 4mm/s2 (peak-to-peak ground amplitude 0.1mm@ 85Hz) in the form of sine function are investigated. The strain changes in the fiber at z-axis are displayed as Figure 4.2.8 and Figure 4.2.9. It can be seen from these two figures that the output waves are subject to distortion within a short period of time.

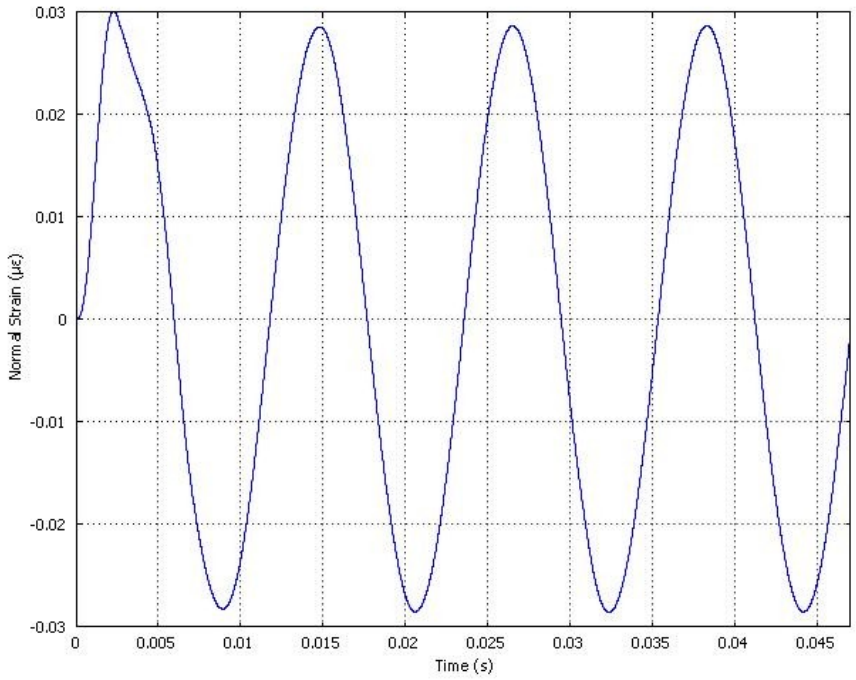

Figure 4.2.8: Normal strain change in the upper fiber of the two-axis accelerometer at z-axis corresponding to 4mm/s2 @85Hz

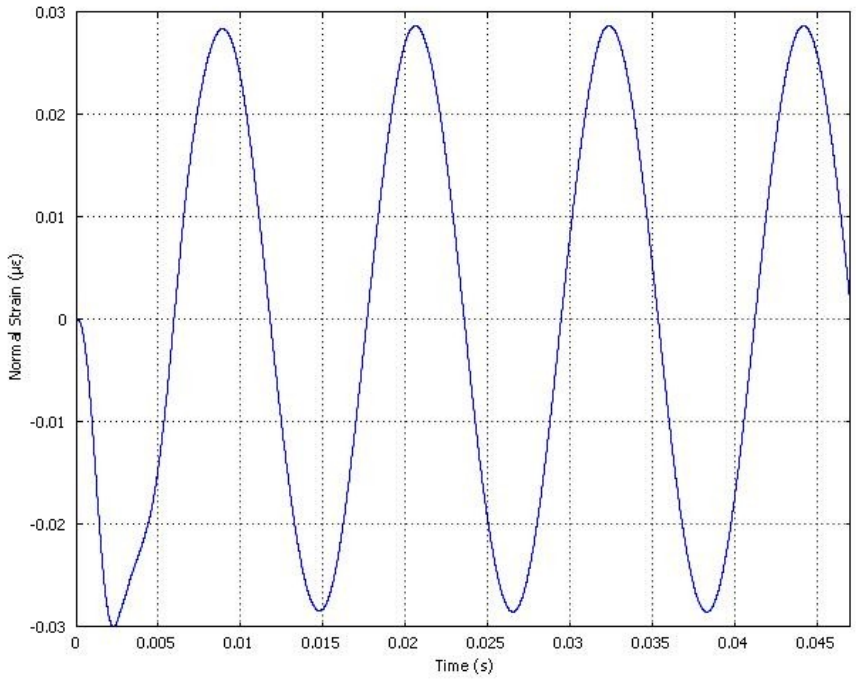

Figure 4.2.9: Normal strain change in the lower fiber of the two-axis accelerometer at z-axis corresponding to 4mm/s2 @85Hz

Then, the strain outputs in the fiber corresponding to the maximum proposed detectable acceleration 40m/s2 at 1Hz in the form of sine function are simulated. The strain changes in the fiber at z-axis are displayed as Figure 4.2.10 and Figure 4.2.11. The peak normal strain change in each portion of the fiber is about 276 $\mu\varepsilon$, which will cause approximately 333.7pm wavelength shift at Bragg wavelength of 1550nm.

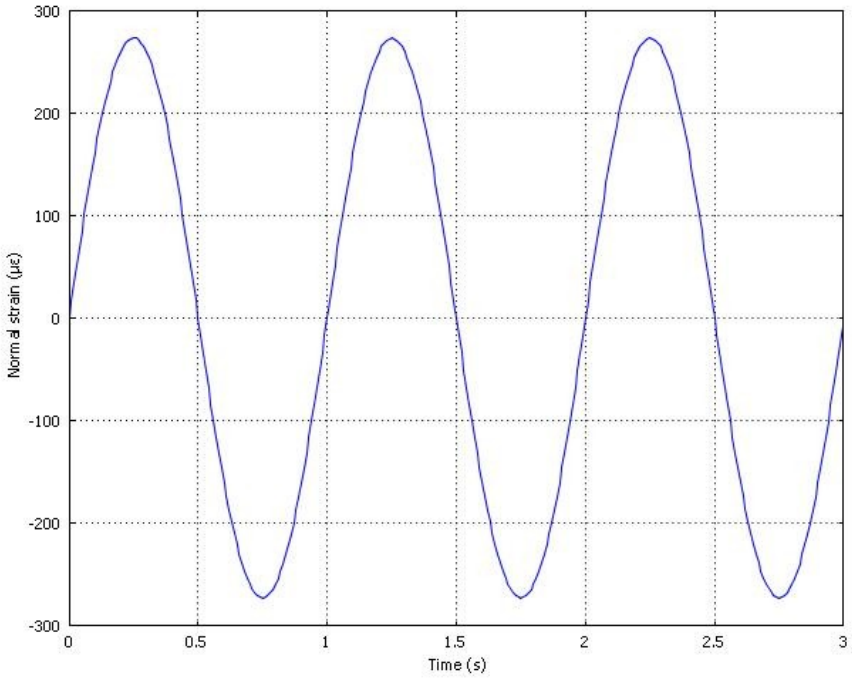

Figure 4.2.10: Normal strain change in the upper fiber at z-axis of the two-axis accelerometer corresponding to 40m/s2 @1Hz

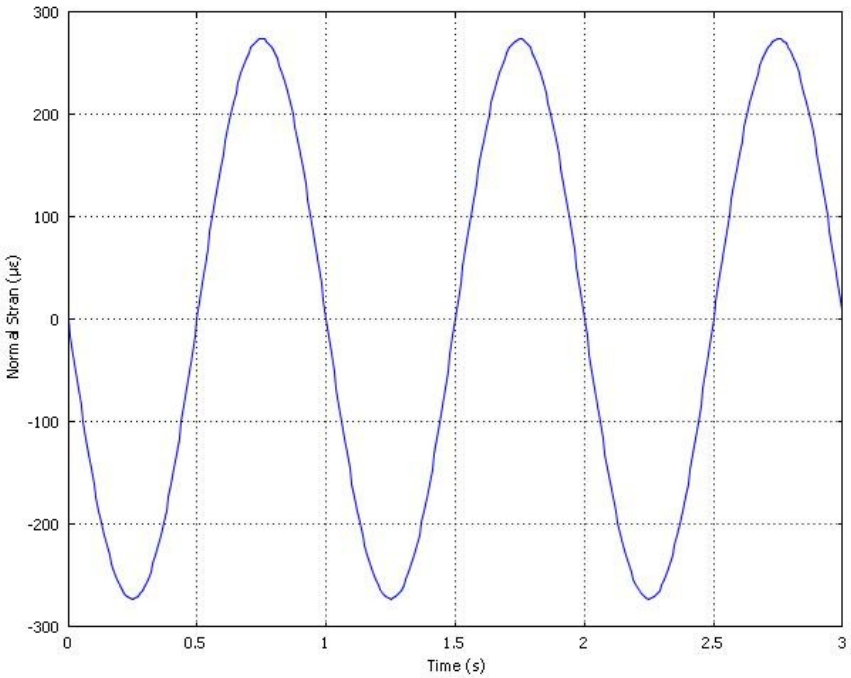

Figure 4.2.11: Normal strain change in the lower fiber at z-axis of the two-axis accelerometer corresponding to 40m/s2 @1Hz

Last, the strain outputs in the fiber corresponding to the maximum proposed detectable acceleration 40m/s2 at 85Hz in the form of sine function are examined as well. The strain changes in the fiber at z-axis are shown as Figure 4.2.12 and Figure 4.2.13. Just like the results obtained at $4mm/s^2$ at 85Hz, the normal strain waves in the upper fiber and in the lower fiber were distorted as well within a very short period of time.

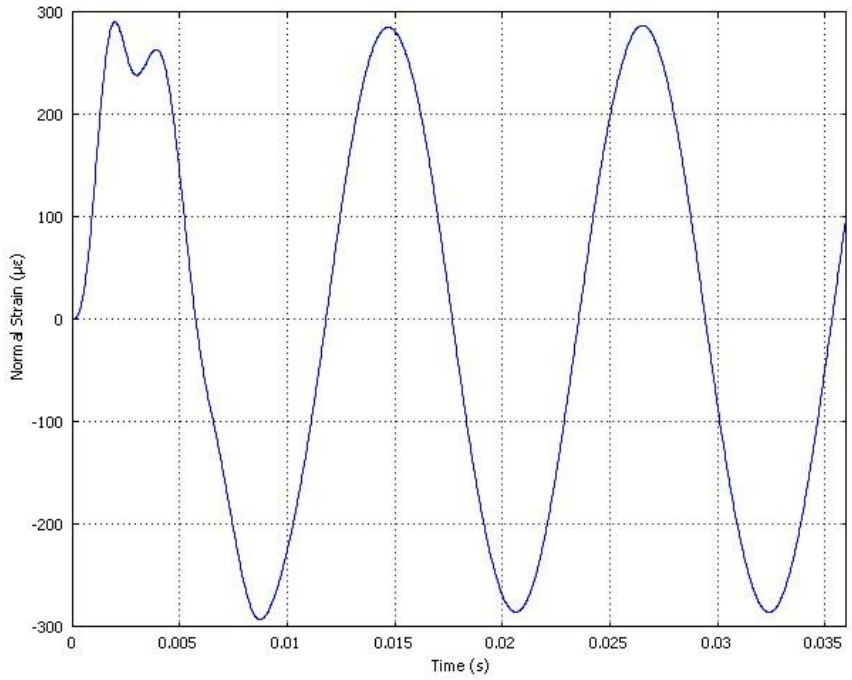

Figure 4.2.12: Normal strain change in the upper fiber at z-axis of the two-axis accelerometer corresponding to 40m/s2 @85Hz

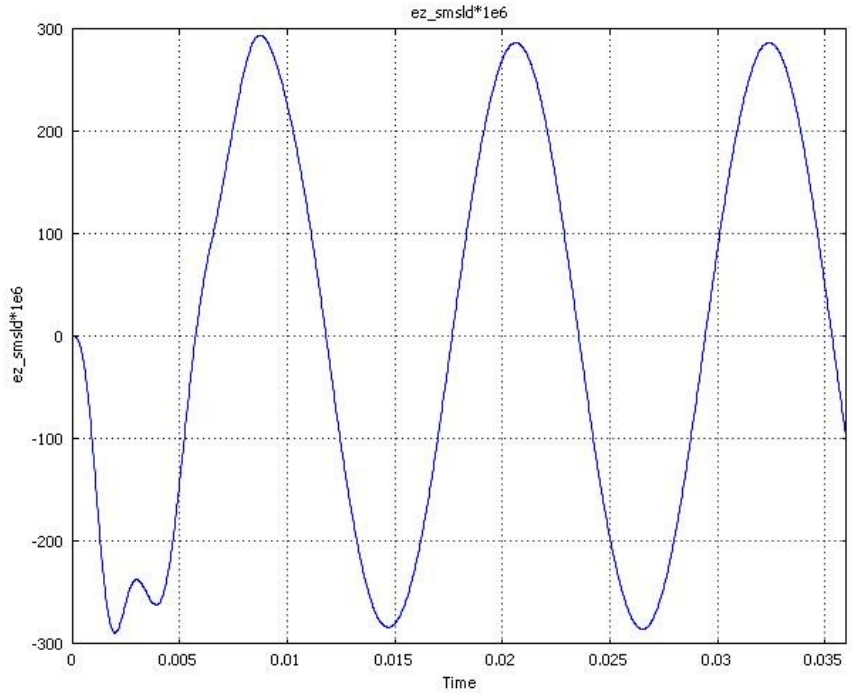

Figure 4.2.13: Normal strain change in the lower fiber at z-axis of the two-axis accelerometer corresponding to 40m/s2 @85Hz

It can be seen from the simulation results that this two-axis transducer has the same outputs corresponding to the excitations with the same amplitude even at different frequencies, which means the excitation force can be deduced from the stain change and the frequency of the force is the frequency of the strain variation within its working frequency (20% of natural frequency).

4.2.3 Strain Distribution

The normal strain distribution over the each fiber section at the sensing axis z is examined. At randomly chosen moments, the strain distribution is uniform over the fiber except at two connection points as shown in Figure 4.2.14. The FBG with length of 1cm written in the middle section of the fiber will only be subject to uniform strain, which to some extent eliminates strain gradient-induced spectral broadening associated with FBG imbedded or attached accelerometers [9]. The x axis represents fiber length at each fiber section while the y axis represents the strain change over the fiber at different moment.

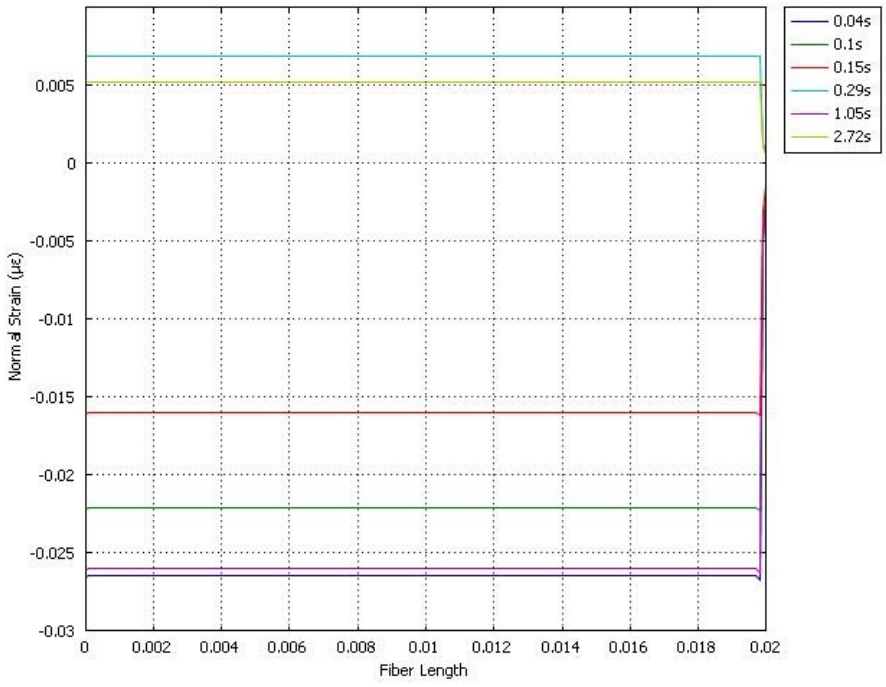

Figure 4.2.14: Two-axis strain distribution over the fiber at 1Hz 4mm/s2 excitation

4.3 Simulation Results of Three-axis Accelerometer

As the simulations done for the two-axis accelerometer, frequency response at each direction, harmonic excitation response, and cross-sensitivity are examined for the three-axis accelerometer as well.

4.3.1 Frequency Response

The three-axis transducer modeled is as per Figure 3.3.1 and the parameters are chosen as per Table 3. The device is free meshed as shown in Figure 4.3.1 in COMSOL Multiphysics. The frequency response for this accelerometer at z-axis is indicated in Figure 4.3.2, Figure 4.3.3, and Figure 4.3.4. The sensitivity of this device is about 23με/g .

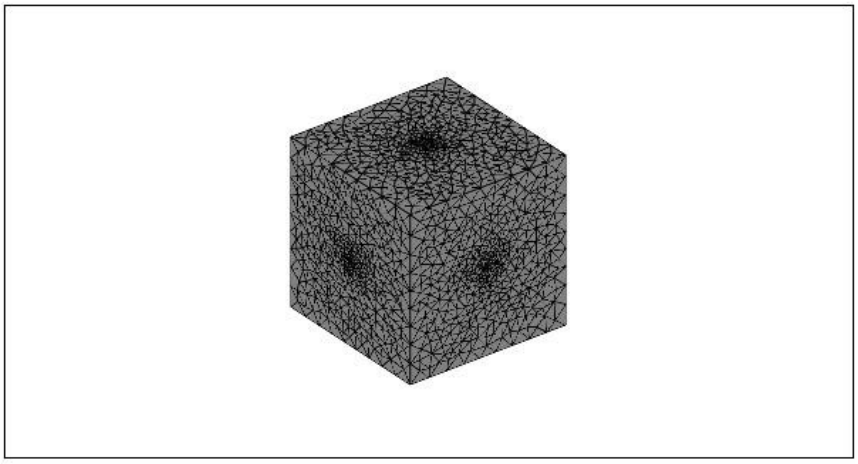

Figure 4.3.1: COMSOL mesh grid of the three-axis transducer

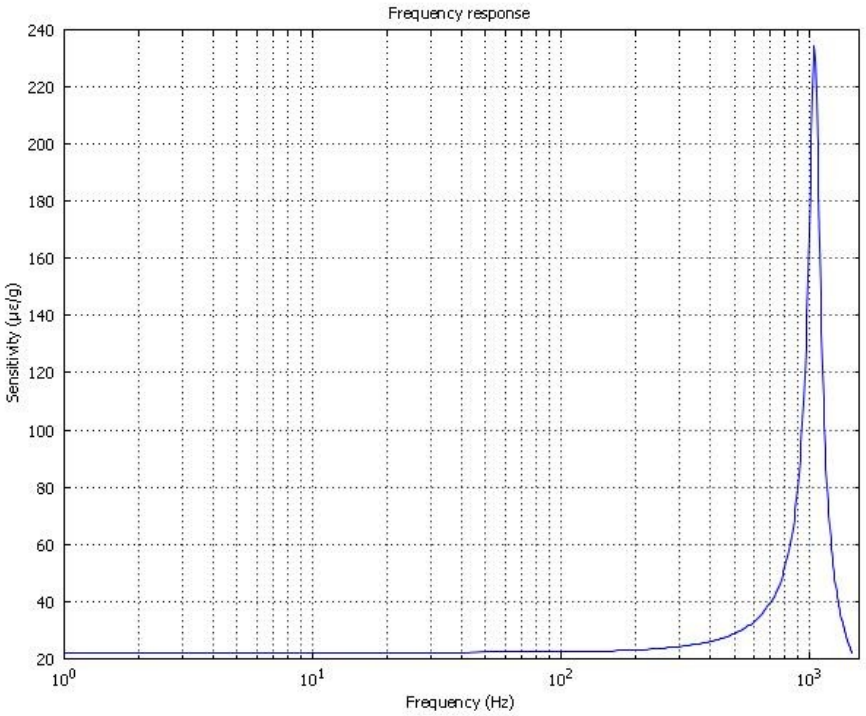

Figure 4.3.2: Sensitivity of the three-axis transducer at z-axis as a function of frequency

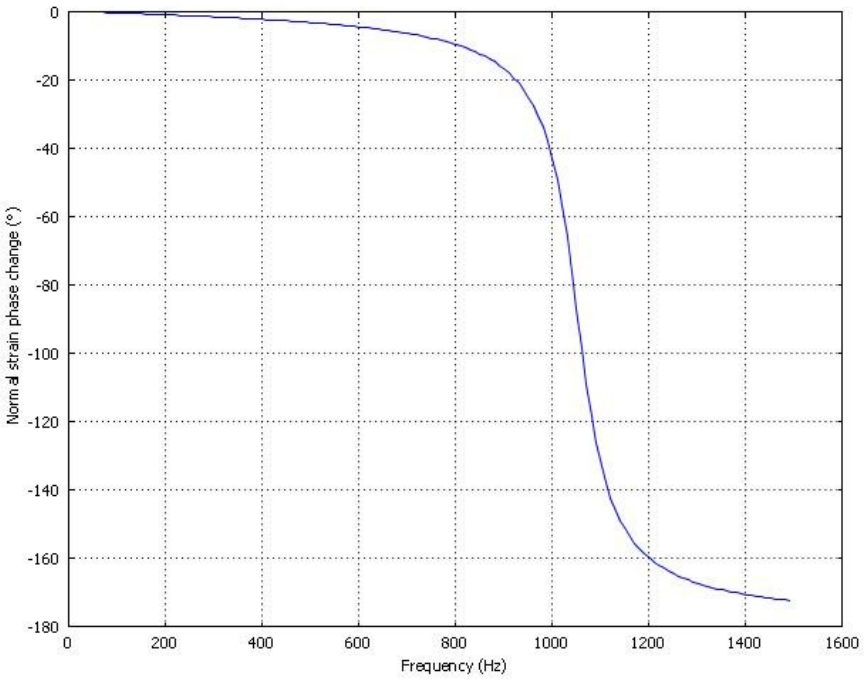

Figure 4.3.3: Phase angle of normal strain in the upper fiber of the three-axis accelerometer at z-axis as a function of frequency

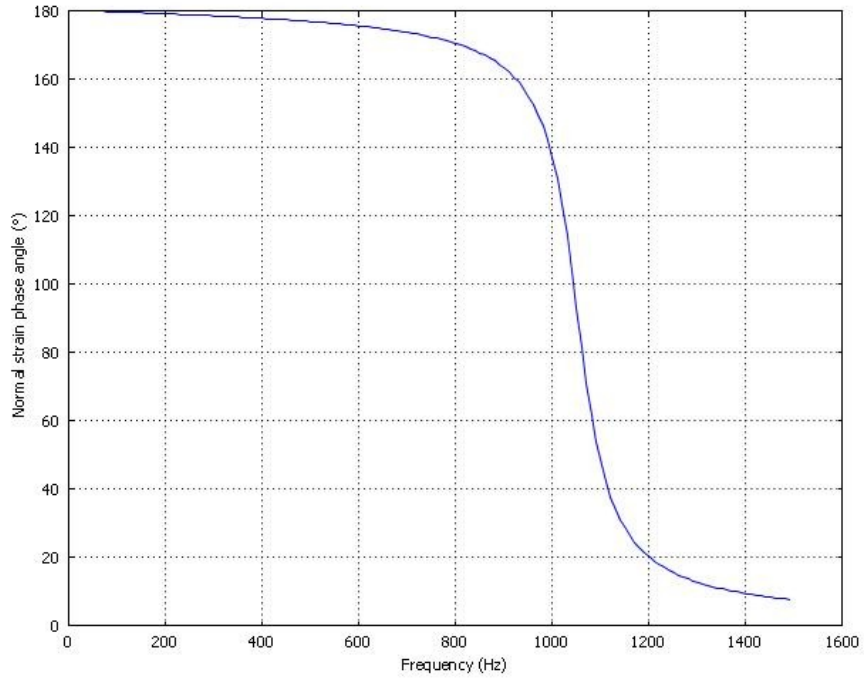

Figure 4.3.4: Phase angle of normal strain in the lower fiber of the three-axis accelerometer at z-axis as a function of frequency

The frequency responses of the three-axis transducer at x-axis and y-axis are illustrated in Figure 4.3.5 and Figure 4.3.6, respectively.

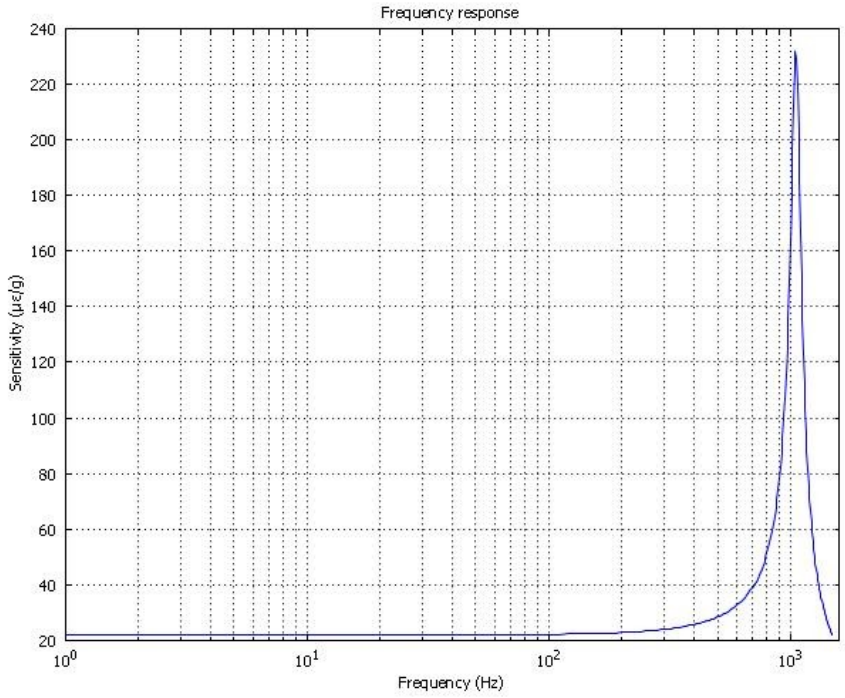

Figure 4.3.5: Sensitivity of the three-axis accelerometer at x-axis as a function of frequency

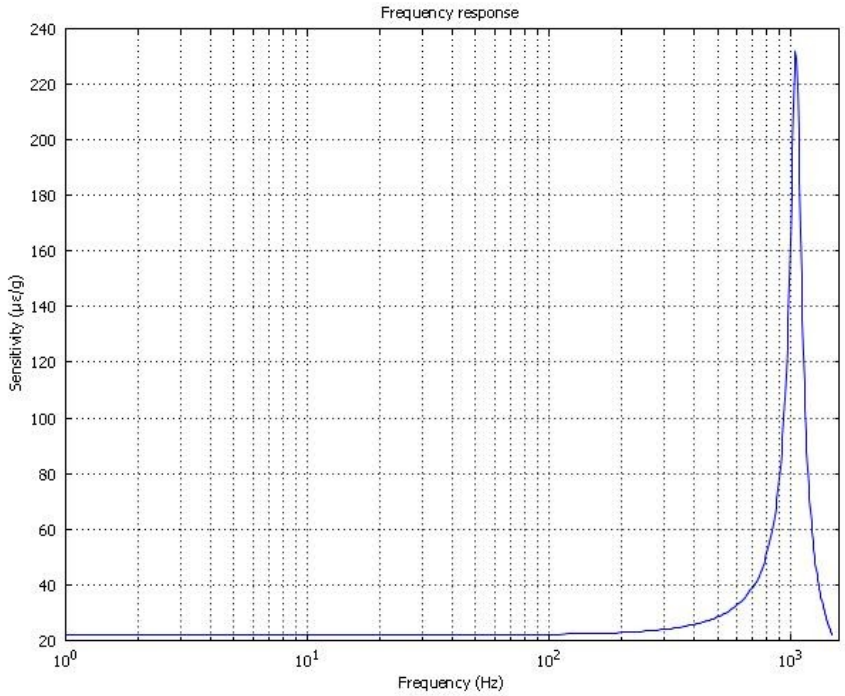

Figure 4.3.6: Sensitivity of the three-axis transducer at y-axis as a function of frequency

The sensitivities from figures shown above at x, y and z axis are the same; therefore, this transducer is capable of detecting acceleration at three different axes with the same detecting mechanism. Similar to the results obtained for the two-axis accelerometer, the simulation results for this device are in good agreement with the theoretical values in terms of natural frequency and phase shift. The natural frequency, where the transducer has highest sensitivity shown in Figure 4.3.2, Figure 4.3.5, and Figure 4.3.6 and has phase shift of $\approx \pm \pi/2$ shown in Figure 4.3.3 and Figure 4.3.4, is quite close to the calculated value 1023Hz.

4.3.2 Harmonic Excitation Response

First, the strain outputs in the fiber corresponding to the lowest resolvable acceleration 4mm/s2 (peak-to-peak ground amplitude 0.1mm@ 1Hz) in the form of sine function are

examined. The normal strain changes in the middle of the upper fiber and of the lower fiber at z-axis are shown in Figure 4.3.7 and Figure 4.3.8, respectively. It is seen that the system oscillates in accordance with the frequency of the excitation. The peak normal strain change is about 4.6e-3 $\mu\varepsilon$, which will cause approximately 0.005pm wavelength shift at Bragg wavelength of 1550nm based on Equation (3.17) as the structure sits in a stable environment. The boundary displacement at t=2.4s is shown as Figure 4.3.9.

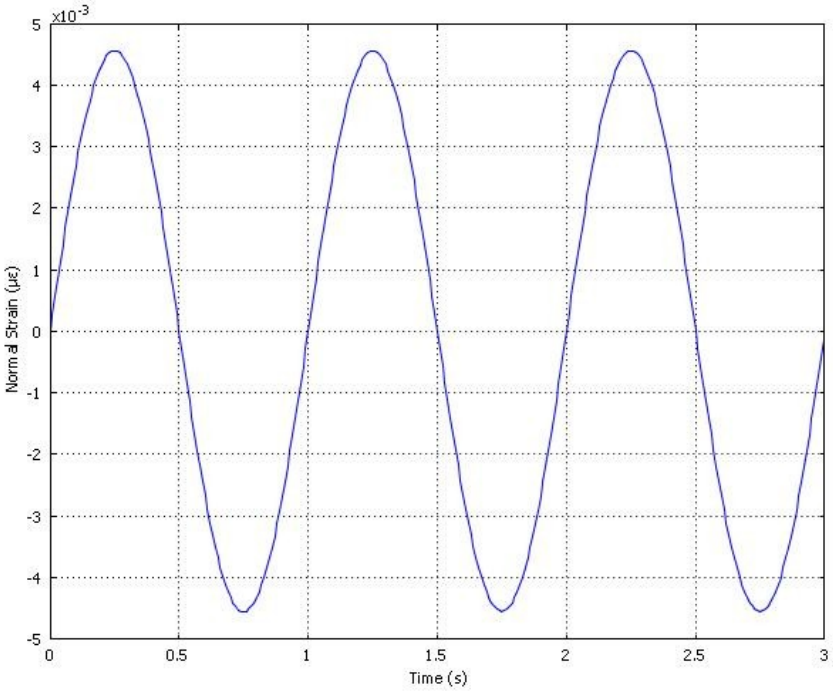

Figure 4.3.7: Normal strain change in the upper fiber of the three-axis accelerometer at z-axis corresponding to 4mm/s^2 @1Hz

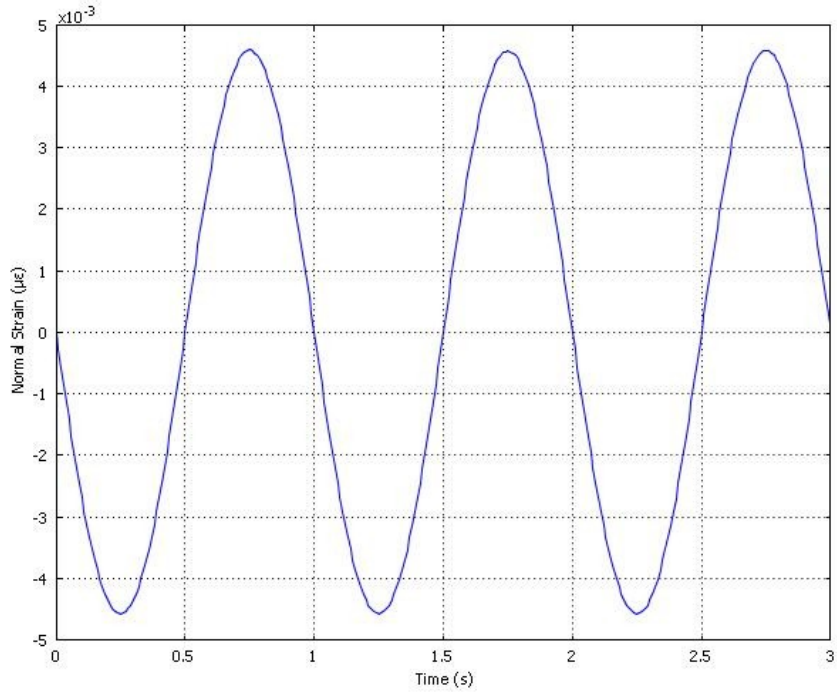

Figure 4.3.8: Normal strain change in the lower fiber of the three-axis accelerometer at z-axis corresponding to 4mm/s^2 @1 Hz

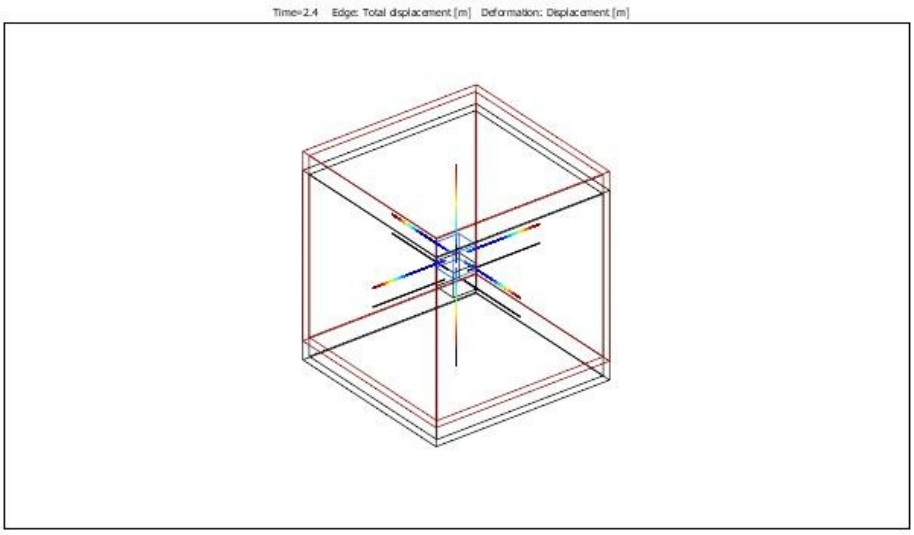

Figure 4.3.9: Boundary displacement at t=2.4s for the three-axis device

Next, the strain outputs in the fiber corresponding to the lowest resolvable acceleration 4mm/s2 (peak-to-peak ground amplitude 0.1mm@ 200Hz) in the form of sine function are investigated. The strain changes in the fiber at z-axis are displayed as Figure 4.3.10 and Figure 4.3.11. The system output is subject to distortion at the initial short period of time.

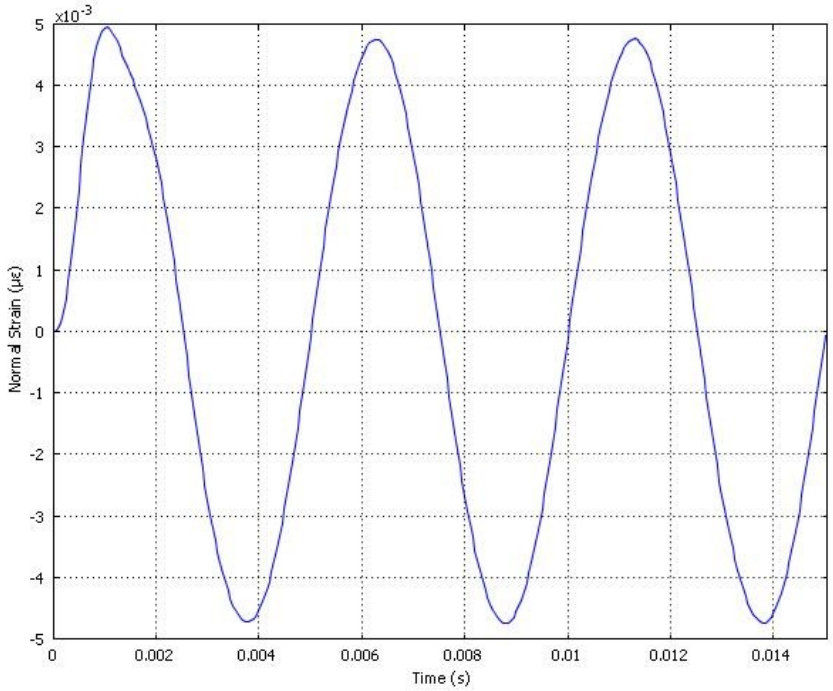

Figure 4.3.10: Normal strain change in the upper fiber of the three-axis accelerometer at z-axis corresponding to 4mm/s^2 @200 Hz

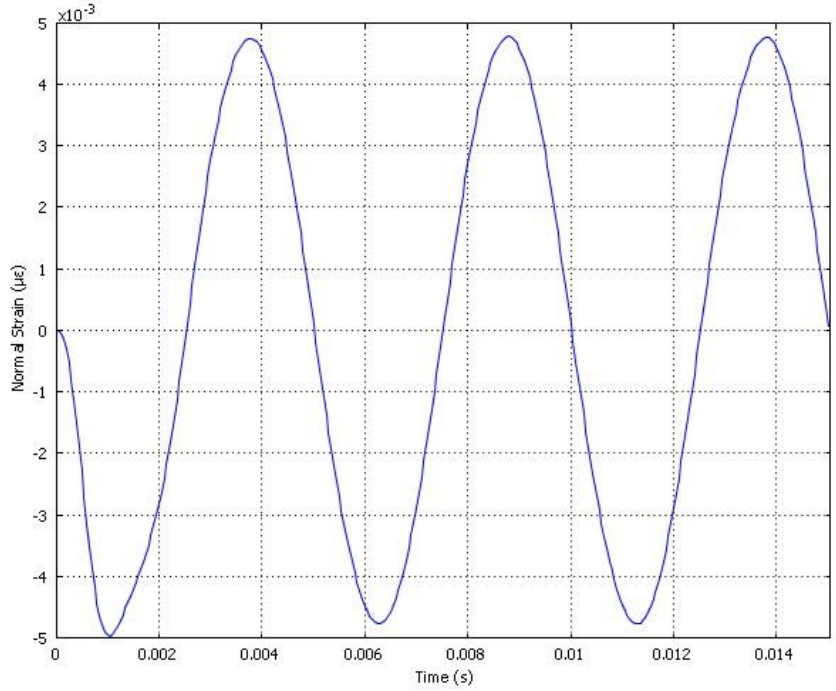

Figure 4.3.11: Normal strain change in the lower fiber of the three-axis accelerometer at z-axis corresponding to 4mm/s2 @ 200Hz

Then, the strain outputs in the fiber corresponding to the maximum proposed detectable acceleration 40m/s2 at 1Hz in the form of sine function are simulated. The strain changes in the fiber at z-axis are show as Figure 4.3.12 and Figure 4.3.13. The peak normal strain change in each portion of the fiber is about $46\,\mu\varepsilon$, which will cause approximately 55.6pm wavelength shift at Bragg wavelength of 1550nm.

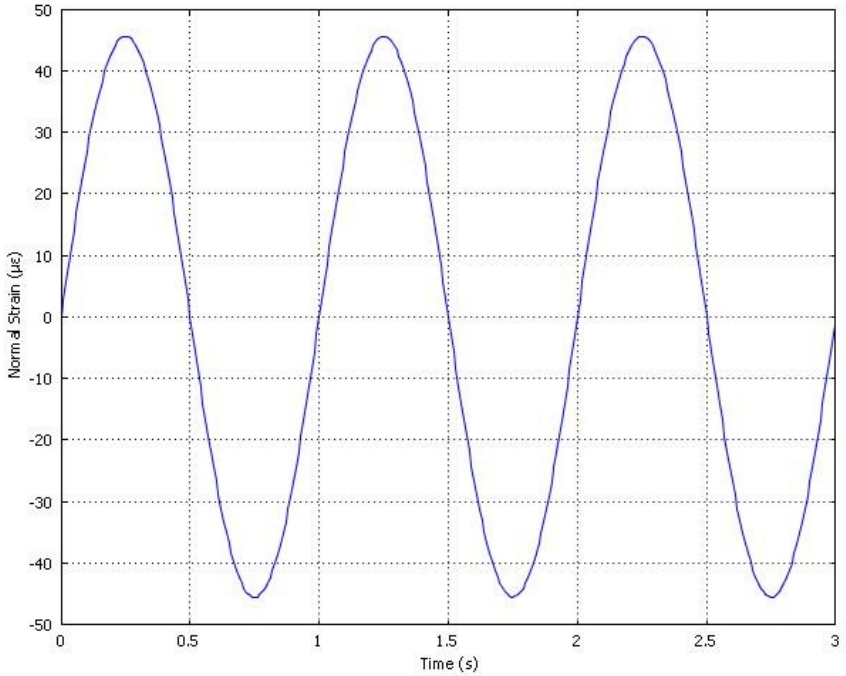

Figure 4.3.12: Normal strain change in the upper fiber of the three-axis accelerometer at z-axis corresponding to 40m/s2 @1Hz

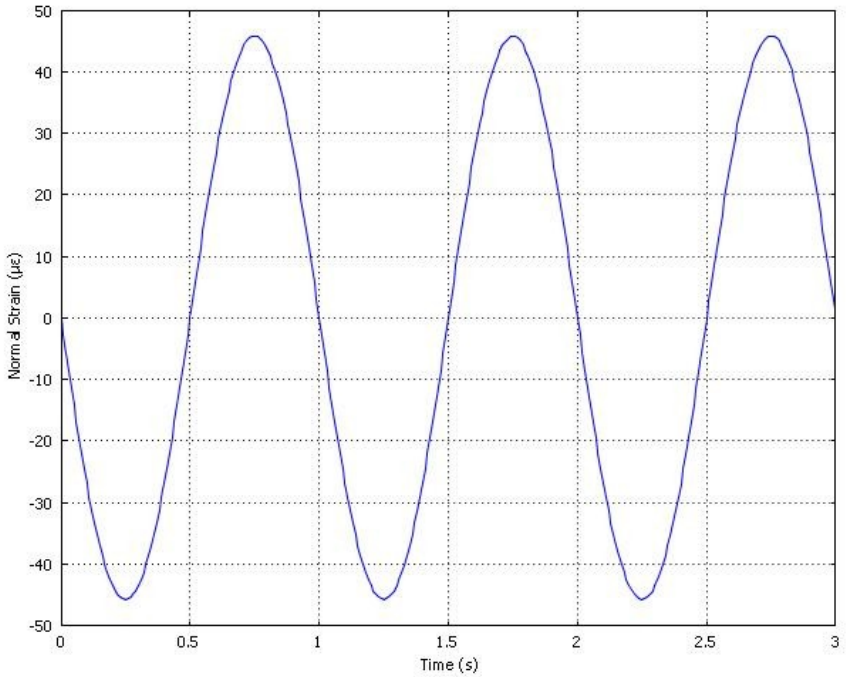

Figure 4.3.13: Normal strain change in the lower fiber of the three-axis accelerometer at z-axis corresponding to 40m/s^2 @1Hz

Last, the strain outputs in the fiber corresponding to the maximum proposed detectable acceleration 40m/s2 at the upper working frequency limit 200Hz in the form of sine function are examined as well. The strain changes in the fiber at z-axis are displayed as Figure 4.3.14 and Figure 4.3.15. In the first half cycle, the output waves are distorted.

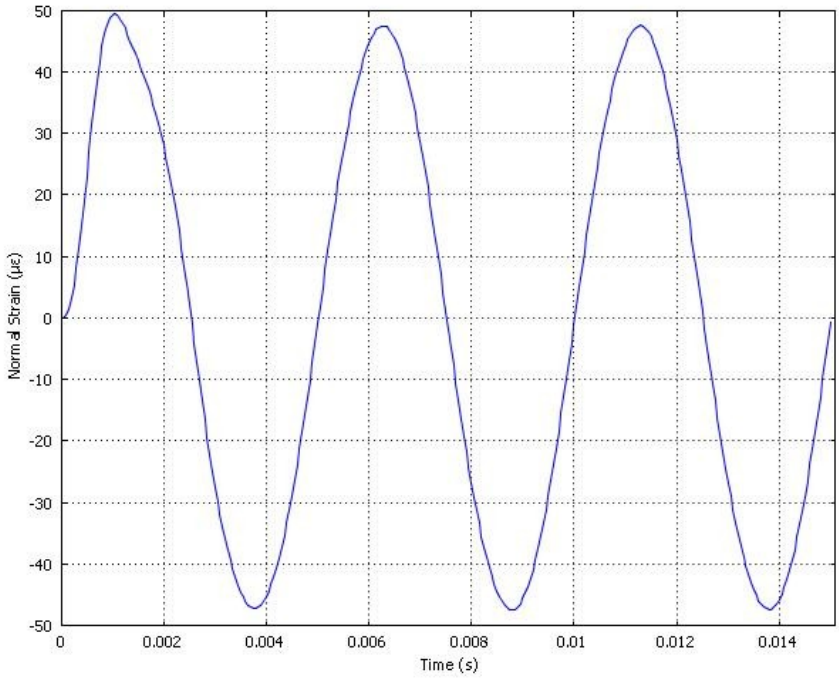

Figure 4.3.14: Normal strain change in the upper fiber of the three-axis accelerometer at z-axis corresponding to 40m/s^2 @200 Hz

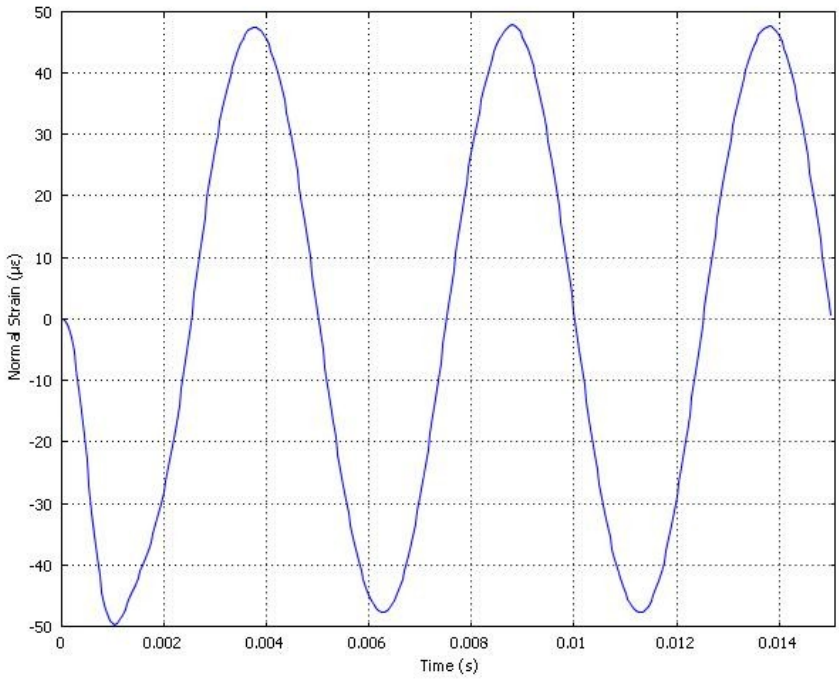

Figure 4.3.15: Normal strain change in the lower fiber of the three-axis accelerometer at z-axis corresponding to 40m/s^2 @200 Hz

It has been demonstrated that the device has uniform outputs between 1Hz and 200Hz in response to the excitation wave with the same amplitude and has a dynamic range of 80dB.

4.3.3 Strain Distribution

The normal strain distribution over the fiber at sensing z-axis is examined. At randomly picked moment, the strain change is uniform except at both ends as shown in Figure 4.3.16. The x axis represents the fiber measuring length at each fiber section and the y axis represents the normal strain output at each picked moment.

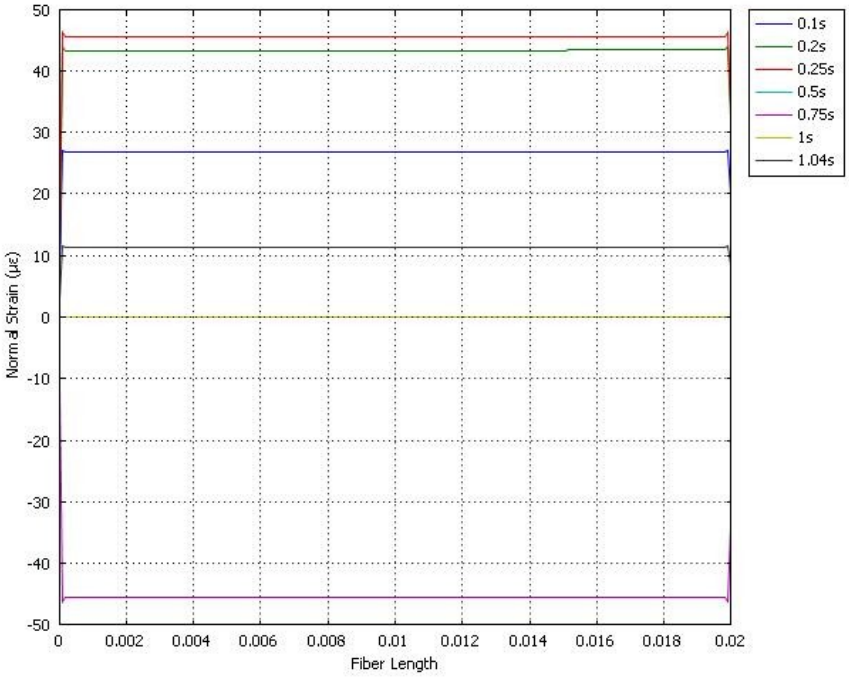

Figure 4.3.16: Three-axis device strain distribution over the fiber to excitation harmonic force of $40m/s^2$ @1Hz

4.3.4 Cross Sensitivity

The normal strain changes at off-axis are shown in Figure 4.3.17 and Figure 4.3.18 when the device is subject to acceleration $40m/s^2$ at 1Hz in z-axis.

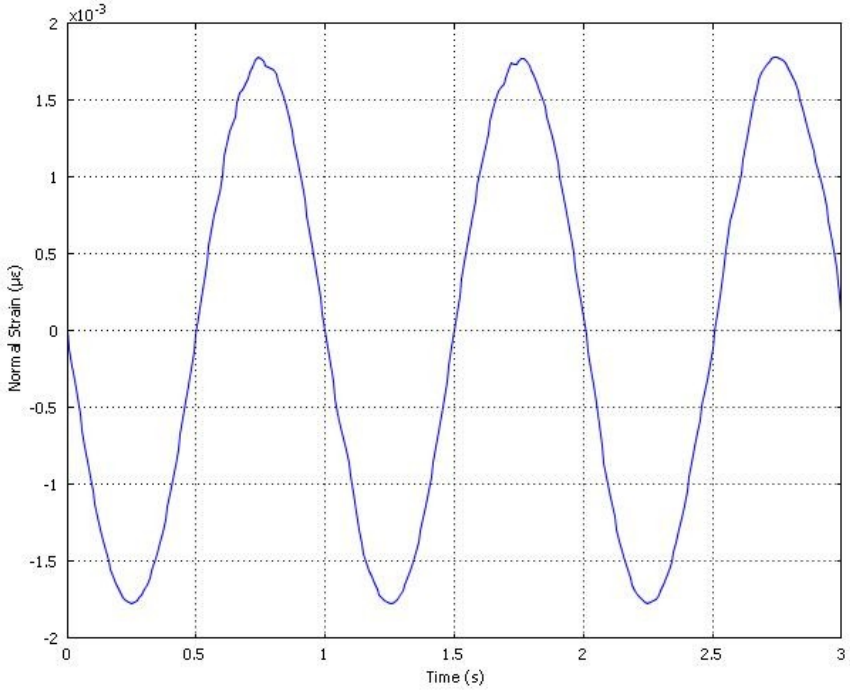

Figure 4.3.17: Normal strain change in the positive direction of the three-axis accelerometer at off-axis

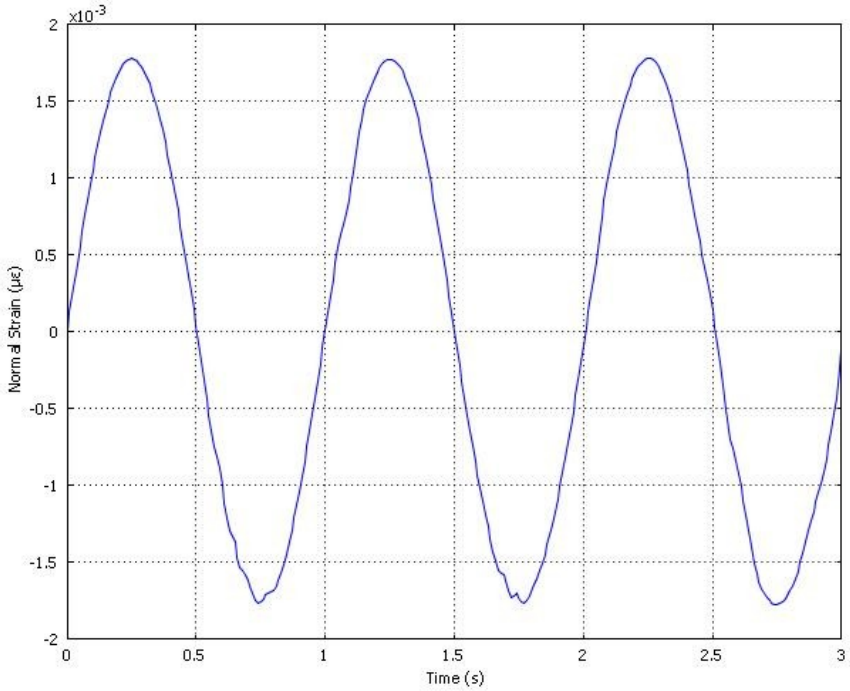

Figure 4.3.18: Normal strain change in the negative direction of the three-axis accelerometer at off-axis

Compared to the peak normal strain changes $46\,\mu\varepsilon$ at the sensing axis z in Figures 4.3.12 and 4.3.13, the cross-sensitivity of this structure is greater than 88dB.

4.4 Results Analysis

From the harmonic responses above, the periodical disturbance force also produces some free vibration of the system. The transient states exist at the beginning of each harmonic excitation response for a very short period of time.

4.4.1 Transient States

The actual motion of the transducer is a superposition of two harmonic motions having different amplitudes and different frequencies, resulting in a very complicated motion, which is more obvious in high frequencies. As a result of damping, after a short time, the free vibration disappears; and only the steady state forced vibrations are left [16]. The common damping ratio 5%, usually used in elastic dynamic analysis in the structures subjected to earthquake motions, is selected for the mathematical modeling.

The complementary solution of Equation (3.6), the standard form of the equation of motion, is the following:

$$\overline{u} = e^{-\omega_n \cdot \zeta \cdot t}(C_1 \cos(\beta t) + C_2 \sin(\beta t)) \tag{4.3}$$

With $\beta = \sqrt{\omega_n{}^2 - (\omega_n \cdot \zeta)^2}$

Equation (4.3) plus the particular solution of Equation (3.7) gives the general solution of the second differential Equation (3.6),

$$u = e^{-\omega_n \cdot \zeta \cdot t}(C_1 \cos(\beta t) + C_2 \sin(\beta t)) + U \sin(\omega t + \varphi) \tag{4.4}$$

U and φ are defined in Equations (3.8) and (3.9), respectively. The amplitude of the transient state depends on the initial conditions of the system. Constants C_1 and C_2 can be solved by placing the initial conditions into Equation (4.4). Here, initial conditions of $u(0) = \dot{u}(0) = 0$ at $t = 0$ are considered,

$$C_1 = -U \sin(\varphi) \tag{4.5}$$

$$C_2 = -\frac{U(\omega_n \cdot \zeta \cdot \sin(\varphi) + \omega \cdot \cos(\varphi)}{\beta} \tag{4.6}$$

If the forcing function is taken to be $a_g = A_g \cos(\omega t)$ instead of $a_g = A_g \sin(\omega t)$, the term $\cos(\omega t)$ replaces $\sin(\omega t)$ in Equation (4.4). If the initial conditions are taken to be $u(0) = \dot{u}(0) = 0$ at $t = 0$, C_1 and C_2 are solved as,

$$C_1 = -U \cos(\varphi) \tag{4.7}$$

$$C_2 = -\frac{U(\omega_n \cdot \zeta \cdot \cos(\varphi) - \omega \cdot \sin(\varphi))}{\beta} \tag{4.8}$$

Therefore, the transient state at the beginning, for a short period of time, showing in the simulation results, was caused by the superposition of free vibration and steady state of the system, and the free vibration is determined by initial conditions.

4.4.2 Thickness of Outside Rigid Case

The thickness of the outside rigid case of the three-axis accelerometer, changed from 0.2mm to 4mm, is modeled while the other parameters remain the same. The sensitivity of this structure doesn't change as per Figure 4.4.2, which means it is an open selection to

choose a rigid case with proper thickness under the consideration of suitable physical strength and a minimum cost.

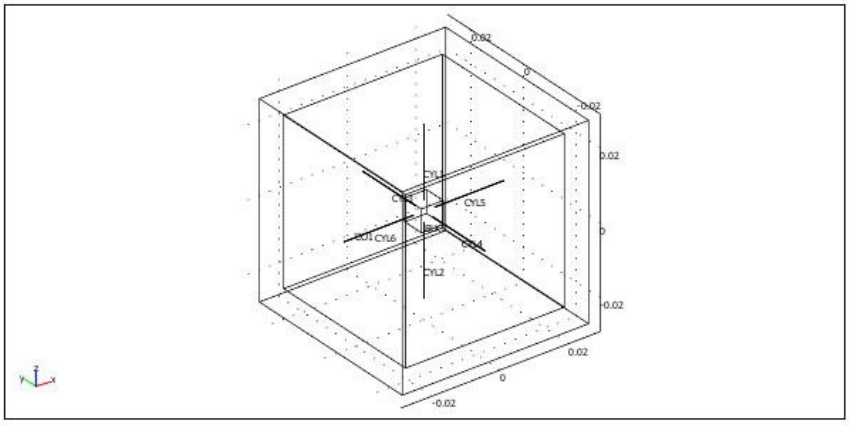

Figure 4.4.1: Three-axis accelerometer with 4mm thick rigid case

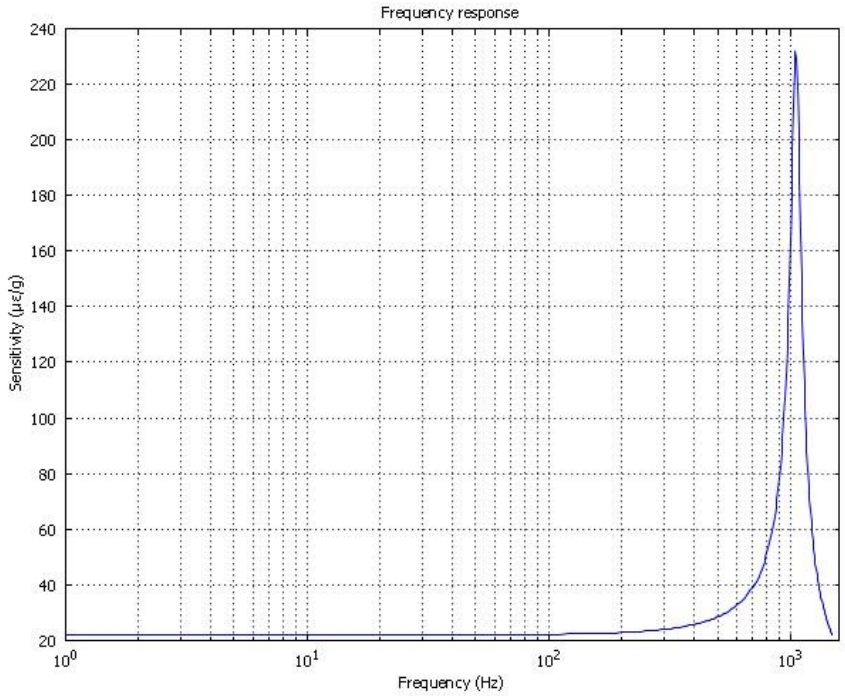

Figure 4.4.2: Sensitivity of the three-axis accelerometer with 4mm thick rigid case

CHAPTER 5 STEP-INDEX FIBER FEM MODELING RESULTS

As FBGs written in the core of step-index fiber, understanding of light traveling through the fiber will be very helpful to visualize light traveling through FBGs. This chapter will only focus on optical fiber modeling with the aid of COMSOL RF Module. FBG modeling is left for future work which can be associated with the receiving system design.

5.1 Modeling Results

A step-index fiber made of silica glass is studied. The refractive index of the inner core is 1.4457. The refractive index of the cladding is 1.4378. The diameter of the core is 8.2 μ m. The diameter of the cladding is 125 μ m, which is chosen to be large enough so that the field of confined modes is zero at the exterior boundaries. The modeling geometry and meshing grid are as Figure 5.1.1 and Figure 5.1.2, respectively.

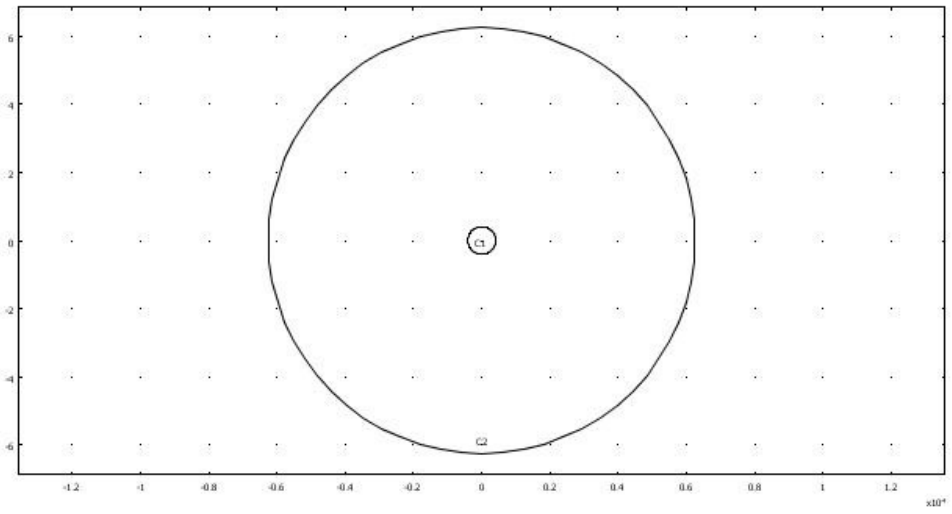

Figure 5.1.1: The modeling geometry of step-index fiber

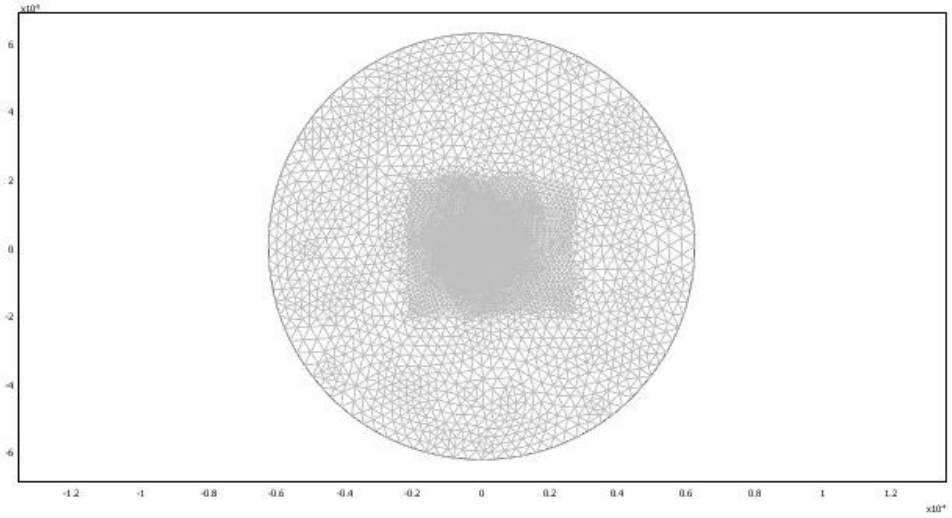

Figure 5.1.2: The meshing grid of step-index fiber

The effective mode index of a confined mode,

$$n_{eff} = \frac{\beta}{k_0} \tag{5.1}$$

as a function of the frequency is an important characteristic. The normalized frequency is defined as:

$$V = \frac{2\pi a}{\lambda}\sqrt{n_1^{\,2} - n_2^{\,2}} \tag{5.2}$$

Where, a is the core radius and λ is the freespace wavelength; n_1 is the refractive index of the core and n_2 is the refractive index of the cladding.

For a confined mode there is no energy flow in the radial direction, thus the wave must be evanescent in the radial direction in the cladding. This can happen only if

$$n_2 < n_{eff} < n_1 \tag{5.3}$$

The waves are more confined when n_{eff} is close to the upper limit in this interval. For this simulation, the effective refractive index for the fundamental mode is 1.442188. The electric and magnetic field for this mode is shown in Figure 5.1.3.

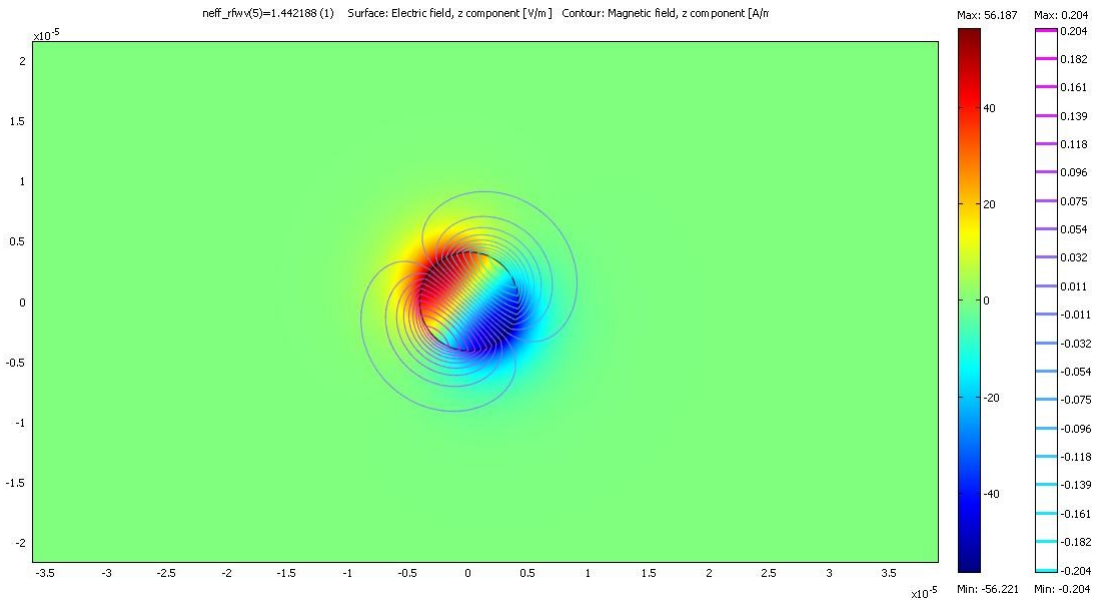

Figure 5.1.3: The electric field and magnetic field at effective index 1.442188

The color scale means the electric field while the contour lines represent the magnetic field. In an ideal optical fiber, the core has a perfectly circular cross-section. In this case, the fundamental mode can be decoupled to two orthogonal polarized modes corresponding to the orientation of the electric field. Two modes with the same effective index travel at the same speed. Figure 5.1.4 shows one mode, and the other polarized mode is represented in Figure 5.1.4.

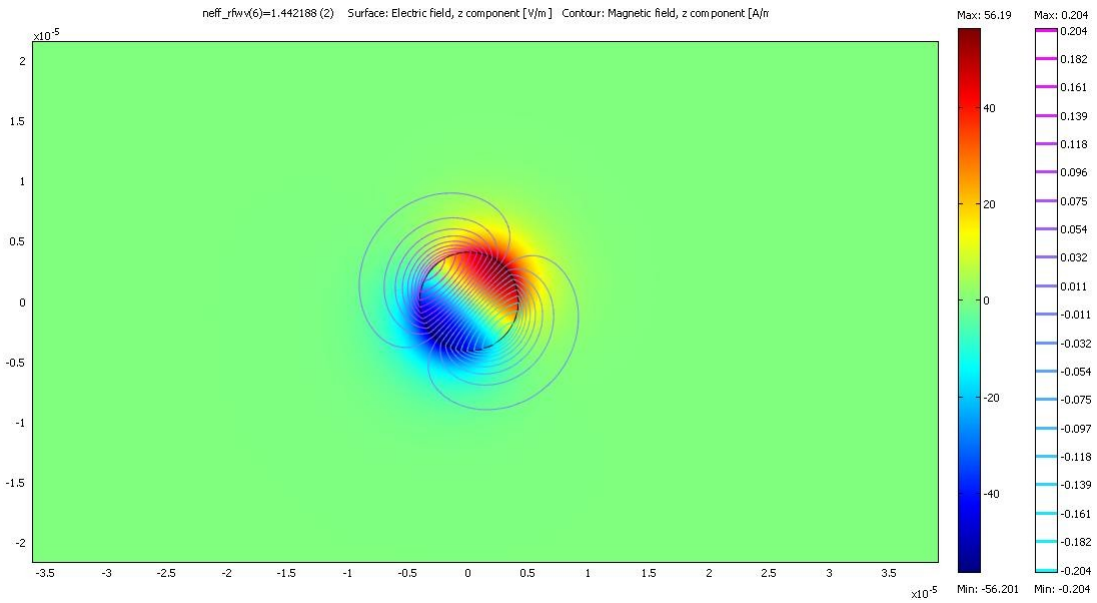

Figure 5.1.4: The electric field and magnetic field at effective index 1.442188 (2)

The surface plot of z-component of the electric field is shown in Figure 5.1.5. The height represents the time average of the power flow.

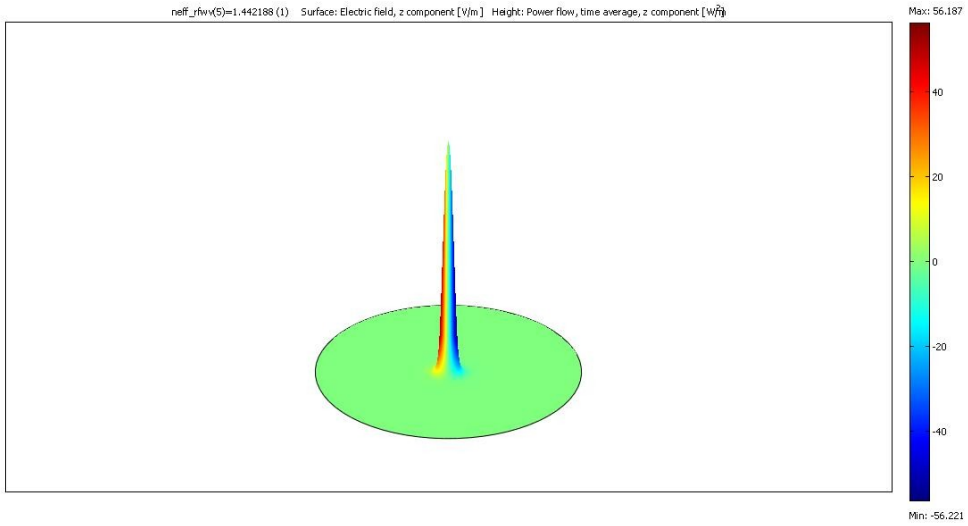

Figure 5.1.5: Surface plot of z-component of the electric field

5.2 Analysis

The critical angle of this fiber is $\theta_c = \sin^{-1}(n_2 / n_1) = 84^0$. Modes are cut off when their rays travel at the critical angle, and rays travel close to 90° almost directly down the fiber. For a given mode, n_{eff} varies with wavelength. At a fixed value of V, several modes might propagate, each having a different effective index. If we put all the parameters (λ=1550nm, α=4.1μm, n_1=1.4457, and n_2=1.4378) into Equation (5.2), the normalized frequency V equals 2.508. Single-mode propagation means only the HE_{11} mode exists and all other modes are cut off. It normally occurs when V<2.405.

The mode that is transmitted over the perfectly circular fiber core is randomly polarized. The modeling results above were obtained by choosing a angle at 86° . In reality, the core of optical fiber is commonly subject to slightly cross-section asymmetry that causes two polarized modes travel at different speed. The speed variety between the two components results in signal broadening.

CHAPTER 6 CONCLUSION AND FUTURE WORK

FBG's have been widely used in various applications in sensors, optical communications and optical signal processing. Great progress has been achieved in the development of fiber-optic accelerometers. Single-axis FBG accelerometers are widely available on the market. A small two-component accelerometer and a three-component accelerometer using single-mode fiber at each axis with FBG written in the core suspended in a proof mass have been developed in this thesis. The proposed sensors have a working frequency range below their resonant frequency, resulting in normal strain changes or Bragg wavelength shifts in proportion to ground acceleration. One single transducer with the capability of detecting multi-axis acceleration will make it very attractive to ocean ground seismic wave monitoring as it can reduce the installation cost and simplify the demodulation system. In order to examine the performance of these two accelerometers, the following simulations and analyses were conducted:

1. Frequency response at all sensing axes was examined. Both the two-axis transducer and the three-axis transducer have a linear frequency response within the frequency range below 20% of the structural natural frequency. The accelerometers are only in proportion to ground acceleration regardless of excitation frequency within its working frequency range. It was noticed that the sensitivity and the bandwidth of the structure is always a trade-off. Wider bandwidth results in lower sensitivity.
2. Response of harmonic excitation (Sine wave) was checked. The outputs of the two transducers shared the same frequency with the forced ground motion, but a transient

state was observed and the wave shape was distorted within a very short time, which is the characteristic of structure motion. The transient state is determined by initial conditions and structure damping.

3. Cross sensitivity at off-axis of the three-axis accelerometer was modeled. The structure has virtually zero cross-sensitivity.
4. Finally, I looked into strain distribution over the entire fiber. The fiber has uniform strain distribution except abrupt strain changes at both ends.

The structures first developed and modeled here proved capability of multi-axis acceleration measuring. The theoretical analysis and the simulation results are in good agreement with each other. The two-axis FBG accelerometer was also proved by experiments performed by one of our group member, Jack Wu. How small we can detect the ground motion also greatly depends, however, on the resolution of the interrogation system. A large variety of approaches have been developed such as, Fabry-Perot bandpass filtering method, interferometer carrier generation, and laser-sensing systems method by others. Using a method which is most appropriate for this application with a balance of attainable performance, implementation complexity and cost would be a fitting effort for future work.

BIBLIOGRAPHY

[1] P. W. Rodgers, A. J. Martin, M. C. Robertson, M. M. Hsu, and D. B. Harris, "Signal Coil Calibration of Electro-Magnetic Seismometers", *Bulletin of Seismological Society of American*; V. 85, No. 3, P. 845-850, June 1995.

[2] T. Aizawa, T. Kimura, T. Matsuoka,T. Takeda, and Y. Asano, " Application of MEMS Accelerometer to Geophysical", *Japanese Committee for Rock Mechanics*, Volume 4, No.2, pp.1-4, 2008.

[3] K.O. Hill, Y. Fujii, D.C. Hohnson, and B. S. Kawasaki, "Photosensitivity in Optical Fiber Waveguide: Application to Reflection Filter Fabrication", *Appl. Phys. Lett.,* Vol. 32, No. 10, 15 May 1978.

[4] G. Meltz G., W.W. Morey, and W.H.Glenn., "Formation of Bragg Gratings in Optical Fibers by Transverse Holographic Method". *Opt. Lett.,* 14:823-825, 1989.

[5] K.O. Hill and G. Meltz, "Fiber Bragg Grating Technology Fundamentals and Overview", *Journal of Lightwave Technology,* Vol.15, No. 8, August 1997.

[6] K. O. Hill, Bragg Grating Fabricated in Monomode Photosensitive Optical Fiber by UV Exposure through a Phase Mask. *Appl. Phys. Letter,* 62(10):1035-1037, 1993.

[7] L. Higuera and J. Miguel, "Handbook of Optical Fibre Sensing Technology", *John Wiley & Sons*, 2002.

[8] K.O. Hill, K.A Vineberg, F.Bilodeau, D.C. Johnson, and I. Skinner, "Efficient Mode Conversion in Telecommunication Fiber Using Externally Written Gratings," *Electron. Lett.*, vol. 26, pp. 1270-1272, 1990.

[9] M. D. Todd, G. A. Johnson, B. A. Althouse, and S. T. Vohra, "Flexural Beam-based Fiber Bragg Grating Accelerometer", *IEEE Photonics Technology Letters*, VOL. 10, NO. 11, NOVEMBER 1998.

[10] A. Mita and I. Yokoi, "Fiber Bragg Grating Accelerometer for Structure Health Monitoring", *Fifth International Conference on Motion and Vibration Control (MOVIC 2000),* Sydney, Australia, 4-8 Dec. 2000.

[11] Y. Zhang, S. G. Li, Z. F. Yin, B.Q Chen, and H. L. Cui, "Fiber-Bragg-grating-based Seismic Geophone for Oil/Gas Prospecting", *Opt. Eng.,* Volume 45, Issue 8, August 2006.

[12] J. C. Palais, "Fiber Optic Communications", *Pearson Education, Inc.,* Fifth Edition, 2005.

[13] S. Z. Yin, P. B. Ruffin, F. T.S.Yu, "Fiber Optic Sensors", *CRC Press*, Second Edition, 2008.

[14] M. J. James, G. M. Smith, J. C. Wolford and P. W. Whaley, "Vibration of Mechanical and Structural Systems", second edition, *Harper Collins College Publishers*, 1994.

[15] D. V. Hutton, "Fundermentals of Finite Element Analysis",*McGraw-Hill*, 2004

[16] W. Weaver, S. Timoshenko, D. H. Young, "Vibration Problems in Engineering", *John Wiley & Sons, Inc*. 1990.